

Design optimisation of piezoelectric energy harvesters for bridge infrastructure

P. Peralta-Braz^a, M. M. Alamdari^a, R. O. Ruiz^b, E. Atroshchenko^{1a}, M. Hassan^c

^a*School of Civil and Environmental Engineering, University of New South Wales, Sydney, Australia*

^b*Department of Civil Engineering, Universidad de Chile, Av. Blanco Encalada 2002, Santiago, Chile*

^c*School of Computer Science and Engineering, University of New South Wales*

Abstract

The use of Piezoelectric Energy Harvesters (PEHs) on bridges is explored in this work. First, a PEH model based on Isogeometric Analysis (IGA) is extended to estimate the harvested energy from induced vibration in bridges using a modal reduction and an efficient time integration method. The model is also coupled with the Particle Swarm Optimisation (PSO) algorithm to find geometry that maximizes energy output. Then, a comprehensive study is conducted to understand the impact of geometry on the PEH performance in a cable-stayed bridge in New South Wales, Australia. The study concludes that tuning the device with one resonance frequency does not guarantee optimal energy generation. Then, a shape optimisation framework is proposed and tested for the field data from the cable-stayed bridge.

Keywords: Piezoelectric Energy Harvester, Parametric Study, Kirchhoff-Love plates, Isogeometric analysis, Shape Optimisation.

1. Introduction

Bridges are a crucial element in transportation systems due to their cost, the connectivity they add to the network, and the severe consequences of their collapse. For this reason, Structural Health Monitoring (SHM) systems on bridges are widely used to ensure safer and more durable bridge structures. In particular, overload is the principal reason leading to the regression of features of bridges. Consequently, monitoring the bridge-crossing traffic is an essential task. Commonly the sensors used for this task are supplied through connecting cables. Nonetheless, cabling can be an inflexible, expensive, and unsafe procedure. Alternatively, wireless sensors powered by chemical batteries require periodic replacement, which can be particularly difficult, expensive, or unfeasible. Recently, vibration energy harvesting has become a promising alternative to provide energy supply for sensors on bridges, taking advantage of kinetic energy induced by the wind load and traffic flow. Particularly, Piezoelectric Energy Harvesters (PEHs) [1, 2] are a widespread and popular option due to their high harvested electrical power density. PEHs are able to convert vibrational energy into electrical power using the direct piezoelectric effect [3]. The most common configuration of PEHs consists of a cantilevered plate composed of a substructure layer and one or two piezoelectric layers. The use of PEHs to harvest energy from the bridge vibrations has been addressed in the literature recently, the most relevant studies are presented below in order to assess their technical feasibility.

¹Corresponding author, e.atroshchenko@unsw.edu.au, eatroshch@gmail.com

A PEH performance on a bridge can be evaluated by performing direct experimental measurements of the produced voltage. In the study by Peigney and Siegert [4], a PEH prototype is tested in situ to quantify the energy generated from traffic-induced vibrations in a pre-stressed concrete highway bridge. From the experimental results, the study's contribution was to propose a design rule for PEHs fitted to bridges based on a simple formulation that relates the energy with the traffic statistics and the parameters of the piezoelectric device. In the same way, Cahill et al. [5, 6] experimentally investigated the performance of two sets of piezoelectric harvesters in a slab double-track rail bridge undergoing forced dynamic vibrations under operational conditions. An accelerometer was installed close to the harvester position in the experimental setup to compare the dynamic response against the generated voltage. Also, a hydraulic shaker was mounted below the bridge deck. The experimental measurements were recorded while the shaker induced a swept sinusoidal force at different amplitudes and frequency ranges in the structure. The paper provides a framework to test the PEH in situ under similar conditions. The authors conclude that it is possible to use the generated voltage to perform modal identification and train passing detection. On the other hand, Zhang et al. [7] tested the piezoelectric energy harvesting from the vibrations induced by vehicle-bridge interactions. An experimental setup is presented to replicate the vehicle-bridge interaction. It consists of a test platform where a scaled vehicle passes. The harvested devices were mounted in different positions under the test platform, and the harvested energy was measured under nine different scenarios. Although the experimental approach provides a reliable estimation of the PEH's performance under real operating conditions, it is limited to testing only a small number of devices since each has to be designed and manufactured. This reduces the design requirement to only tune the device to one of the relevant bridge frequencies. In [4], the prototype's resonance frequency was designed to target the resonance vibration of a structure attached to the bridge. In [5, 6], the two sets of PEHs were designed with resonance frequencies to target the first two modes of the bridge. In [7], the two PEHs were designed with different fundamental frequencies, one with the bridge's natural frequency and the other with the frequency of a vehicle-bridge coupling vibration. While this can lead to satisfactory results, they are not necessarily optimal. Peigney and Siegert [4] elaborate on this. From the proposed formulation that related the delivered power according to the traffic intensity, the authors state that the piezoelectric device studied is not optimal, opening the discussion of designing a PEH that maximises energy production.

Other studies have addressed the problem with a theoretical approach, presenting mathematical and numerical models for the vehicle-bridge interaction coupled with the PEH. Karimi et al. in [8] proposed a model of the vehicle-bridge interaction (VBI) system, modeled as an Euler-Bernoulli beam under a point mass moving with a constant speed to estimate the vibrations at a particular structure point. Next, the VBI model is coupled with a PEH model to estimate the amount of produced voltage. PEH is also modelled as the Euler-Bernoulli beam. Next, the authors experimentally validate the mathematical model of PEH. The experimental validation concluded that the proposed model has a good agreement and can be used to design piezoelectric devices for bridges. In the same direction, Song [9] investigated the application of PEH in railway bridges numerically. The author proposed a finite element analysis-based model for PEH, which is deduced from Hamilton's principle. The model is used to simulate a unimorph-type harvesting device. Two pre-stressed concrete (PSC) girder bridges were designed and simulated for the study, one single-span and another double-span. The simulation estimated the vertical acceleration response of a moving train at several bridge points. The moving train load was considered as a train of 20 cars, with speeds varied with simulations. After evaluating different device's positions and train speeds, it is concluded that the generated energy is enough to power wireless devices. On the other hand, Romero et al. [10] studied the performance of

the piezoelectric harvesters on railway bridges under different train circulating passes conditions. An approximation model based on modal superposition estimates the energy generated from train-induced bridge vibrations by a PEH. Experimental data measured in situ in a railway bridge from a High-Speed line is used in the study. A time window of three and a half hours and twenty train passages is evaluated in the mathematical model to quantify the harvested energy. The authors conclude that the amount of energy depends strongly on traffic intensity and the PEH design. Therefore, a numerical model provides greater versatility in designing and selecting a device than experimental studies. However, a common approach in the mentioned works is to model the PEHs based on the Euler-Bernoulli beam theory, even though PEHs are designed and manufactured as thin structures more similar to plates than beams. The first PEH model based on the Kirchhoff-Love plate and Hamilton's generalised principle for electrostatic bodies was presented in [11]. The model was solved numerically using the finite element method, and the obtained results showed an agreement with the experimental data. Later, Peralta et al. [12] presented an Iso-Geometric Analysis (IGA) framework for a PEH based on the Kirchhoff-Love plate. The two main advantages of the IGA-PEH model are its capacity to parametrise the shape of the device by B-Splines, allowing complex configurations with many design parameters, and its high accuracy due to the high continuity of the B-Spline basis functions. In addition, in terms of computational time, the IGA-based framework is faster than FEM analysis with the same accuracy, which is an essential advantage in the optimisation problem that requires generating a large number of iterations. Later, in [13], the model was extended to devices of variable thickness. Thus, the IGA PEH model was chosen for the present study. The model was integrated with the vibration histories from a bridge SHM data to estimate the amount of the produced voltage. Subsequently, a comprehensive parametric study was carried out to understand how the geometry of the devices affects their performance and give general guidelines for design. Then the model was coupled with the optimisation algorithm to find the design configurations with the maximum power outcome.

The works mentioned previously agree on the potential feasibility of using PEH to supply electrical power to electronics commonly used for structural health monitoring in bridges. In [8], the reported RMS voltage is between 0.4–8.0 mV. The study indicates that the voltage is almost proportional to the speed increment of the vehicle. In [4] it is reported that for the peak intensity of traffic, the power reaches 0.03 mW with a voltage between 1.8 and 3.6 V, indicating that it is enough to supply wireless health monitoring nodes with a low duty cycle. In [7], the higher device's efficiency was achieved when it was installed in the middle of the bridge. The PEHs harvested 579 μJ energy each time. In [9], the RMS value of the output voltage varies between 0.5–205 V among all the sceneries of bridge vibrations. The energy varies between 8.0–462 μJ . In the most favourable case, the authors indicate that the energy scavenged by one PEH is enough to power a wireless intelligent sensor and actuator network node. In [10], the generated energy from a time window of three and a half hours and twenty train passages is 3.6 mJ. The authors suggest storing the produced energy and using it in intermittent measurement operations. However, the design process has not been addressed in-depth in the mentioned research. In general, design is limited to synchronising the resonant frequency of the device with one of the natural frequencies of the bridge. However, as previously discussed in other studies [14, 15, 12, 13], the shape of the device has a high impact on its performance. Therefore, proposing an optimisation framework to improve efficiency can contribute to its widespread use.

The contributions of this work are summarise as follows:

- The IGA-PEH model, developed in [12] for a single harmonic acceleration input, is extended for an arbitrary base acceleration using the modal reduction and time integration methods. The model is also coupled with the Particle Swarm Optimisation (PSO) algorithm to find geometric

configurations with the maximum energy output. The study is limited to rectangular geometries with constant thickness, but the extension to more complex designs parameterised by B-Splines is straightforward. To the best of our knowledge, this is the most accurate and versatile PEH model available in the literature.

- A detailed parametric study is performed to evaluate the effect of the damping ratio and electrical resistance on the produced power. An additional optimisation algorithm is implemented in the model to chose the value of the electrical resistance with the highest power outcome.
- Shape optimization is performed for the field SHM data from a cable-stayed bridge in New South Wales. Hence, this work represents the first study on PEH design optimization for the real operational conditions.

The remainder of the paper is organised as follows. The theoretical framework of the PEH model is reviewed in Section 2. In Section 3, the cable-stayed bridge employed in this work is presented, and the data collection process is explained. In Section 4, a modal order reduction and time integration process are proposed to estimate the voltage generated from the bridge, where numerical results are verified against experimental measurements. In order to understand the behaviour of the PEH on bridges, some parametric studies and shape optimisation analyses are carried out in Section 5. Next, an optimisation framework for PEH on bridges is presented in Section 6. Finally, a study case is employed in Section 7 to show the framework's potential in the design process. Conclusions are presented in Section 8.

2. PEH Modeling: Time Integration

2.1. IGA Model for PEHs

The PEH modeled in this section corresponds to a bimorph-type device which is a well-known and ample studied configuration in the literature. The main architecture of the PEH corresponds to a cantilevered plate composed of three layers. The middle layer, also called substructural layer, is made of a non-piezoelectric material that serves as structural support for the plate. This layer is considered rectangular with length L , width W and thickness h_s . Here, two layers made with piezoelectric ceramics are bonded to the substructural layer, as shown in Figure 1, and connected in series to an external electrical resistance R_l . The piezoelectric layers' thickness is denoted by h_p . Note that piezoelectric layers cover the substructure only partially (the corresponding length is denoted by L_{pzt}). The domains occupied by the piezoelectric layers Ω_p and the substructure Ω_s are defined by

$$\Omega_p = \left((0, L_{pzt}) \times (0, W) \times \left(\frac{h_s}{2}, \frac{h_s}{2} + h_p \right) \right) \cup \left((0, L_{pzt}) \times (0, W) \times \left(-\frac{h_s}{2} - h_p, -\frac{h_s}{2} \right) \right) \quad (1)$$

$$\Omega_s = \left((0, L_{pzt}) \times (0, W) \times \left(-\frac{h_s}{2}, \frac{h_s}{2} \right) \right) \cup \left((L_{pzt}, L) \times (0, W) \times \left(-\frac{h_s}{2} - h_p, \frac{h_s}{2} + h_p \right) \right) \quad (2)$$

while the material domain of the device is given by

$$\Omega = \Omega_s \cup \Omega_p \quad (3)$$

Note that the most common architectures studied in the literature consider the piezoelectric layers covering the substructural layer entirely, i.e. $L_{pzt} = L$, see for instance [12]. Additionally, it is also common to incorporate a tip mass, facilitating the tuning of the device at lower frequencies

and increasing the vibration amplitude, hence, the energy harvested. However, and for the sake of simplicity, it is decided to work with PEHs without tip masses. On the other hand, the motivation to work with substructural layers partially covered is to add another design variable that can potentially leads to a better performance. This is explored later in Sections 4 and 5.

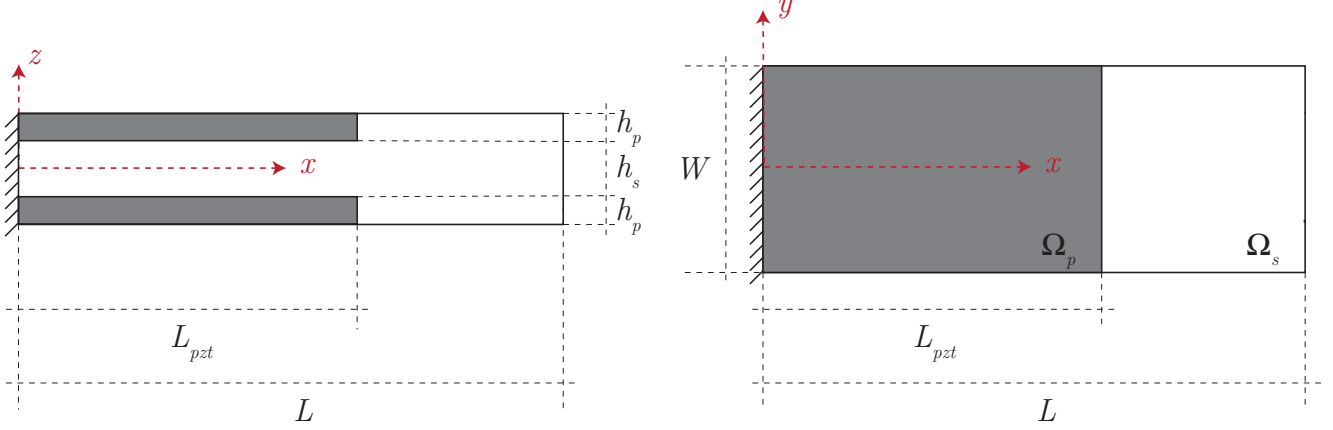


Figure 1: Architecture of the piezoelectric energy harvester, corresponding to a cantilever plate, consisting of two piezoelectric layers bonded to a main substructure.

The mathematical model for the PEH is deduced from the Generalised Hamilton's principle for electro-elastic bodies and Kirchhoff-Love plates. Details of this model are given in [12], hence, only the main formulation is presented here. The constitutive equation for the substructure is given by

$$\mathbf{T} = \mathbf{c}_s \mathbf{S}, \quad (4)$$

where \mathbf{T} , \mathbf{S} , and \mathbf{c}_s , correspond to the mechanical stress tensor, the mechanical displacement vector and the elastic stiffness matrix, respectively. On the other hand, the constitutive equation for the piezoelectric material is given by

$$\begin{Bmatrix} \mathbf{T} \\ \mathbf{D} \end{Bmatrix} = \begin{bmatrix} \mathbf{c}_p^E & -\mathbf{e}^T \\ \mathbf{e} & \boldsymbol{\epsilon}^S \end{bmatrix} \begin{Bmatrix} \mathbf{S} \\ \mathbf{E} \end{Bmatrix} \quad (5)$$

where \mathbf{D} is the electrical displacement vector, \mathbf{E} is the electrical field vector, \mathbf{c}_s^E is the elastic stiffness matrix at constant electric field, \mathbf{e} is the piezoelectric constant matrix, and $\boldsymbol{\epsilon}$ is the permittivity components matrix at constant strain.

The shape of the PEH is described by B-Splines N_I and the deflection field $w(\mathbf{x})$ is approximated, according to provisions of the isogeometric analysis (IGA), using the same basis functions N_I as follow

$$\mathbf{x}(\boldsymbol{\xi}) = \sum_{I=1}^k N_I(\boldsymbol{\xi}) \tilde{\mathbf{x}}_I, \quad (6)$$

$$w(\boldsymbol{\xi}, t) = \sum_{I=1}^k N_I(\boldsymbol{\xi}) w_I(t), \quad (7)$$

where \mathbf{x} is an arbitrary material point inside the domain Ω , I is a bivariate index, $\boldsymbol{\xi} = (\xi, \eta)$ is the parametric coordinate ($\xi, \eta \in [0, 1]$), $\tilde{\mathbf{x}}_I$ represents a control point of the control mesh, and $w_I(t)$ is

the deflection projected at control point I . Substituting equation (6) and equation (7) into the weak form of the problem, the following coupled system of algebraic equations is obtained:

$$\mathbf{M}\ddot{\mathbf{w}} + \mathbf{C}\dot{\mathbf{w}} + \mathbf{K}\mathbf{w} - \mathbf{\Theta}v_p = \mathbf{F}a_b \quad (8)$$

$$C_p\dot{v}_p + \frac{v_p}{R_l} + \mathbf{\Theta}^T\dot{\mathbf{w}} = 0 \quad (9)$$

Equation (8) corresponds to the mechanical equation with electrical coupling while equation (9) corresponds to the electrical circuit equation with mechanical coupling, where $\mathbf{w} \in \mathbf{R}^{N \times 1}$ is a vector containing the deflections $w_I(t)$, $v_p = v_p(t)$ is the output voltage, $a_b = a_b(t)$ is the acceleration imposed at the base of the PEH, $\mathbf{M} \in \mathbf{R}^{N \times N}$ is the mass matrix, $\mathbf{K} \in \mathbf{R}^{N \times N}$ is the stiffness matrix, $\mathbf{C} = \alpha\mathbf{M} + \beta\mathbf{K} \in \mathbf{R}^{N \times N}$ is the mechanical damping matrix (where α and β are the proportional damping coefficients), $\mathbf{F} \in \mathbf{R}^{N \times 1}$ is the mechanical forces vector, $\mathbf{\Theta} \in \mathbf{R}^{N \times 1}$ is the electromechanical coupling vector, C_p is the capacitance, and R_l is the external electric resistance. The matrices \mathbf{M} , \mathbf{K} , \mathbf{F} and $\mathbf{\Theta}$ are assembled as

$$M_{IJ} = \int_{\Omega_s} \rho_s (N_I N_J + z^2 N_{I,x} N_{J,x} + z^2 N_{I,y} N_{J,y}) d\Omega_s + 2 \int_{\Omega_p} \rho_p (N_I N_J + z^2 N_{I,x} N_{J,x} + z^2 N_{I,y} N_{J,y}) d\Omega_p \quad (10)$$

$$K_{IJ} = \int_{\Omega_s} z^2 \mathbf{B}_I^T \mathbf{c}_s \mathbf{B}_j d\Omega_s + 2 \int_{\Omega_p} z^2 \mathbf{B}_I^T \mathbf{c}_p^E \mathbf{B}_j d\Omega_s \quad (11)$$

$$\Theta_I = \int_{\Omega_p} z \mathbf{B}_I^T \mathbf{e}^T \mathbf{Z} d\Omega_p \quad (12)$$

$$F_I = \int_{\Omega_s} \rho_s N_I d\Omega_s + \int_{\Omega_p} \rho_p N_I d\Omega_p + \sum_{J=1}^k \int_{\Omega_s} \rho_s z^2 (N_{I,x} N_{J,x} + N_{I,y} N_{J,y}) d\Omega_s + \sum_{J=1}^k \int_{\Omega_p} \rho_p z^2 (N_{I,x} N_{J,x} + N_{I,y} N_{J,y}) d\Omega_p \quad (13)$$

where ρ_s is the substructure density, ρ_p is the piezoelectric material density, while \mathbf{B}_I and \mathbf{Z} are defined as

$$\mathbf{B}_I = \begin{Bmatrix} -N_{I,xx} & -N_{I,yy} & -2N_{I,xy} \end{Bmatrix}^T \quad (14)$$

$$\mathbf{Z} = \begin{Bmatrix} 0 & 0 & \frac{1}{h_p} \end{Bmatrix}^T \quad (15)$$

From equations (8) and (9), also considering that excitation and response are harmonic signals of the form $a_b(t) = A_b e^{i\omega t}$ and $v(t) = V_o e^{i\omega t}$ (where $i = \sqrt{-1}$), it is possible to define the Frequency Response Function (FRF) that relates the amplitudes of the output voltage V_o and the excitation acceleration A_b for a specific frequency ω . The FRF is defined as follows

$$H_v(\omega) = \frac{V_o(\omega)}{A_b} = i\omega \left(\frac{1}{R_l} + i\omega C_p \right)^{-1} \tilde{\mathbf{\Theta}}^T \left(-\omega^2 \mathbf{M} + j\omega \mathbf{C} + \mathbf{K} + i\omega \left(\frac{1}{R_l} + i\omega C_p \right)^{-1} \tilde{\mathbf{\Theta}} \tilde{\mathbf{\Theta}}^T \right)^{-1} \mathbf{F} \quad (16)$$

The FRF, given by equation (16), characterises the dynamic response of a PEH subjected to a harmonic excitation (acceleration at the base of the PEH). However, when the PEH is intended to be used for real applications, the excitation of the PEH could potentially differs from a harmonic signal. As consequence, base the design of PEHs on equation 16 could lead to sub-optimal designs.

To circumvent this limitation, it is necessary to extend the modeling process to enable the study of any arbitrary excitation, i.e., performing the time integration of equations (8) - (9). Time integration is a computationally intensive process, then, if an optimisation requires to perform a time integration to evaluate the objective function, the problem could become computational intractable (in particular for long time series). In order to reduce this computational burden, the IGA model is coupled with a Modal Order Reduction, which is discussed next.

2.2. Modal Order Reduction for Time Integration

Here, a Modal Order Reduction (MOR) [16] is applied to the system described by equations (8)-(9). This method allows reducing the degrees of freedom of the system, considering only a limited number of free vibration modes to represent the dynamic behaviour in a specific frequency range. Free vibration modes can be found from equation (8), considering that the device is unforced, undamped, and unpolarised, i.e.

$$\mathbf{M}\ddot{\mathbf{w}} + \mathbf{K}\mathbf{w} = \mathbf{0} \quad (17)$$

Then, a harmonic representation of the deflection leads to the generalised eigenvalue problem

$$(\mathbf{K} - \omega_i^2 \mathbf{M})\phi_i = \mathbf{0} \quad (18)$$

Here, $\phi_i \in \mathbf{R}^{N \times 1}$ represents the mode shape vectors and ω_i are the undamped natural frequencies. The deflection solution \mathbf{w} can be approximated through a truncated expansion of the first K mode shape vectors, associated with the first K natural frequencies:

$$\mathbf{w} \approx \mathbf{w}_o = \Phi_o \boldsymbol{\eta} \quad (19)$$

where $\mathbf{w}_o \in \mathbf{R}^{N \times 1}$ is the approximate deflection solution, $\Phi_o \in \mathbf{R}^{N \times K}$ is the matrix which contains the K first mode shape vectors ϕ_i and $\boldsymbol{\eta} \in \mathbf{R}^{K \times 1}$ denotes the modal coordinates. In this way, it is possible to define the reduced mass matrix \mathbf{m}_o :

$$\mathbf{m}_o = \Phi_o^T \mathbf{M} \Phi_o \quad (20)$$

Next, equations (8) and (9) can be represented in modal coordinates and normalised by the reduced mass matrix resulting in a reduced-order system

$$\ddot{\boldsymbol{\eta}} + \mathbf{c}_o \dot{\boldsymbol{\eta}} + \mathbf{k}_o \boldsymbol{\eta} - \boldsymbol{\theta}_o v_p = \mathbf{f}_o a_b \quad (21)$$

$$C_p \dot{v}_p + \frac{v_p}{R_l} + \boldsymbol{\Theta}^T \Phi_o \dot{\boldsymbol{\eta}} = 0 \quad (22)$$

where

$$\begin{aligned} \mathbf{c}_o &= \mathbf{m}_o^{-1} \Phi_o^T \mathbf{C} \Phi_o = \begin{bmatrix} 2\zeta_1 \omega_1 & & \\ & \ddots & \\ & & 2\zeta_K \omega_K \end{bmatrix} \\ \mathbf{k}_o &= \mathbf{m}_o^{-1} \Phi_o^T \mathbf{K} \Phi_o = \begin{bmatrix} \omega_1^2 & & \\ & \ddots & \\ & & \omega_K^2 \end{bmatrix} \\ \boldsymbol{\theta}_o &= \mathbf{m}_o^{-1} \Phi_o^T \boldsymbol{\theta} \\ \mathbf{f}_o &= \mathbf{m}_o^{-1} \Phi_o^T \mathbf{F} \end{aligned} \quad (23)$$

Note that the new stiffness and damping matrices, \mathbf{k}_o and \mathbf{c}_o (equation 23), are now defined in terms of the undamped natural frequencies ω_i and the damping ratios ζ_i associated to the modes of interest $\{i = 1, \dots, K\}$.

The voltage generated by the piezoelectric devices comes from the solution of the system of differential equations given by equations (21) and (22). This system of equations is solved adopting an explicit Runge-Kutta method, i.e. Dormand-Prince method [17], and employing an acceleration record as excitation. Ultimately, the procedure allows to efficiently estimate (by considering only a small subset of vibration modes) the time history of the generated voltage given a known excitation.

2.3. Verification of the MOR Model for PEHs

Although the modal order reduction method decreases the computational time required to estimate the output voltage, it has an approximation error compared to the full order model. Thus, it is necessary to seek a balance between accuracy and computational time. This issue is studied here and corresponds to the verification of the MOR model, i.e., how credible is the MOR model in comparison with the model with full degrees of freedoms. A specific PEH is selected to analyse the impact of the number of vibration modes on time and accuracy. The geometrical parameters and the electromechanical properties of the device are given in tables 1 and 2, respectively. The study is carried out adopting the excitation shown in Figure 2, in the context of this work, the excitation will be called event. This excitation corresponds to an acceleration time history recorded in the cable-stayed bridge adopted in Section 5 as a case of study. The final outcome of the model is the amount of energy harvested, denoted by $E(\mathbf{x}|e)$, where vector \mathbf{x} defines the PEH's geometry (i.e., L , L_{pzt} , W , h_p and h_s) and e is the event identification. This notation explicitly indicates that the energy harvested depends on the geometry of the devices and the excitation time history (event). Ultimately, the estimation of the energy harvested is obtained from the numerical integration of the power signal $P(t, \mathbf{x}|e) = v^2(t, \mathbf{x}|e)/R_l$, i.e.

$$E(\mathbf{x}|e) = \int_{t_1}^{t_2} P(t, \mathbf{x}|e) dt = \int_{t_1}^{t_2} \frac{v^2(t, \mathbf{x}|e)}{R_l} dt \quad (24)$$

Table 1: Geometrical characteristics of the PEH employed in the verification of the MOR model. The PEH is considered without tip mass.

Length (L)	200	[mm]
Length Piezoelectric Layer(L_{pzt})	200	[mm]
Width(W)	200	[mm]
Piezoelectric Thickness (h_p)	0.25	[mm]
Substructure Thickness (h_s)	0.50	[mm]

Figure 3a shows the estimated energy harvested and its relative error (with respect to the full model of 255 degrees of freedom) for different number of modes. On the other hand, in Figure 3b, the dependence of the computational time respect to the number of modes is shown. As expected, reducing the number of modes decreases both, the computational time and accuracy. Therefore, thirty vibration modes will be considered in all numerical studies in this work since it provides the error of less than 3% and a computation time of less than 2s. The voltage signal estimated by the model considering thirty modes for event (presented in figure 2) is presented in Figure 4.

Table 2: Substructure and piezoelectric mechanical and electromechanical properties for the PEH employed in the verification of the MOR model.

Substructure Young's modulus, E_s	105	[GPa]
Substructure density, ρ_s	9000	[kg/m ³]
Substructure Poisson's ratio, ν	0.3	
Piezoelectric layer density, ρ_p	7800	[kg/m ³]
Permittivity	$1800 \times \epsilon_0$	[nF/m]
c_{11}^E, c_{22}^E	120.3	[GPa]
c_{12}^E	75.2	[GPa]
c_{13}^E, c_{23}^E	75.1	[GPa]
c_{33}^E	110.9	[GPa]
c_{66}^E	22.7	[GPa]
e_{31}^E, e_{32}^E	-5.2	[C/m ²]
e_{33}^E	15.9	[C/m ²]

2.4. Validation of the MOR Model for PEHs

In this section the MOR model is compared with experimental data employing a commercial bi-morph PEH. Hence, the validation answer the following question: how adequate are the IGA and MOR models to describe the physics involved in the problem. Note that the verification performed previously answer a different question: what is the accuracy of the MOR model respect to the full model. In the experiment performed, the harvester is attached to an electromagnetic shaker such that any given excitation can be imposed. The harvester's piezoelectric layers are connected in series to a single electrical resistance of 1000 Ω , forming an electrical circuit. An acquisition system is set to record the voltage $v(t)$ at the electrical resistant and the excitation acceleration $a_b(t)$ at the base of the PEH. This experimental setup is implemented following the directions offered in [18].

Table 3 presents the electromechanical properties and the geometric characteristics of the PEH used in the validation. The identification of these properties for the commercial PEH was carried out using the Bayesian inference framework proposed by Peralta et al. (for more details, see ref. [19]).

Figure 5a shows the pulse acceleration (excitation) recorded at the base where the commercial PEH is clamped. On the other hand, in Figure 5b, the blue line corresponds to the experimental measurement of the generated voltage given the pulse excitation imposed. The pulse acceleration recorded is used as excitation in the numerical simulation (using the MOR model with $K = 30$), the respective response is plotted in Figure 5b with a yellow dotted line. As can be seen in Figure 5b, the numerical simulation is in agreement with the experimental results indicating the suitability of the proposed model to estimate the voltage response in the PEH.

3. Optimisation of PEHs for Bridge Applications based on Time Series Excitations

This section proposes an optimisation framework for designing a PEH to maximise the power generation for in service bridges. The framework requires to record the acceleration of the bridge at the possible location of the PEH. This data should be recorded in a time window large enough that can be taken as a representative behaviour of the bridge response. The acceleration recorded is

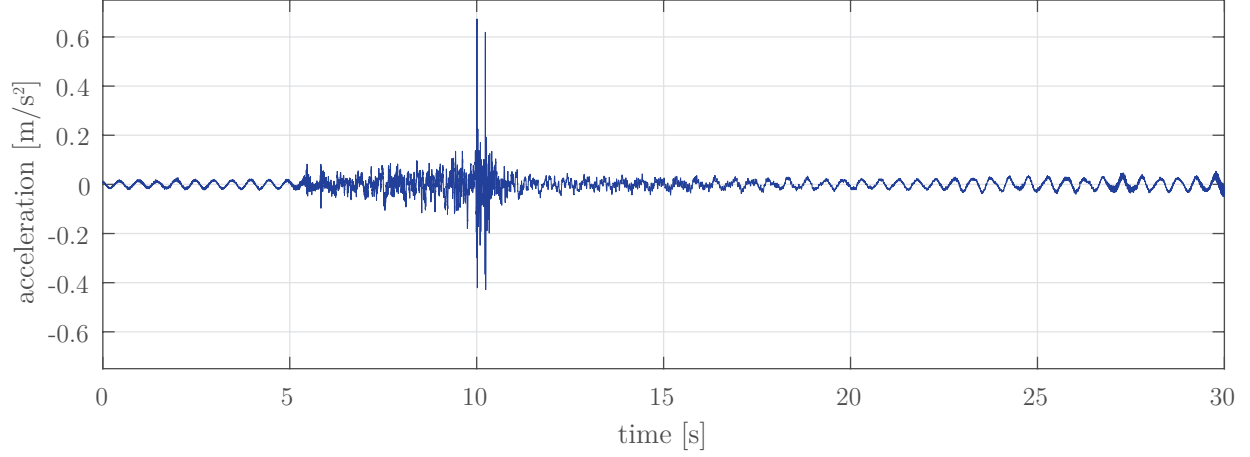


Figure 2: Excitation employed to perform the verification of the MOR model. This event corresponds to an acceleration time history of the cable-stayed bridge used in Section X as case of study. This event has been labeled as event 2.

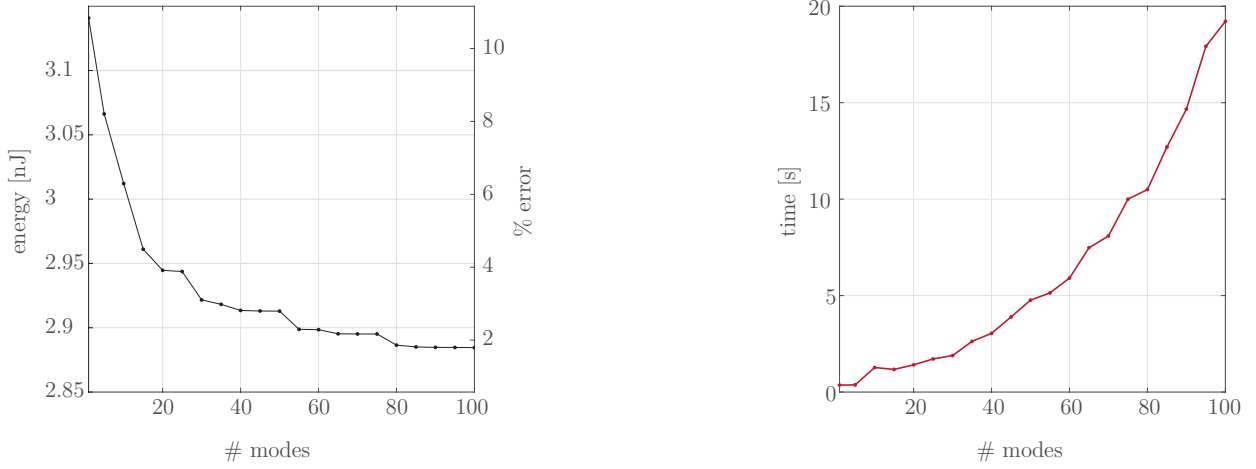


Figure 3: Estimated energy harvested and relative simulation error (with respect to the full model) for different number of modes (left). Computational time for different number of modes (right)

taken as the excitation of the PEH. The treatment and manage of this excitation is presented in the following section. Afterwards, the main steps of the proposed optimisation are detailed.

3.1. Excitations Required by the Optimisation

In a first instance, it is required to extract single events from the record of accelerations. Here, an event is defined by spikes of accelerations, such that accelerations greater than a certain threshold indicate the presence of an event. An event can be caused by environmental conditions or by the passage of vehicles over the bridge, however in this framework, no distinctions are made regarding the cause. An example of a single event is presented in Figure 2 where an acceleration threshold is set equal to 0.2m/s. Here, the event time window is fixed to 30s and the location of the peak acceleration is forced to be at 10s. In this regard, it is required to identify all events contained in the acceleration record. Note that all events will have the same time window and the same location for the peak acceleration. The events will be labeled with a number corresponding with the order of detection.

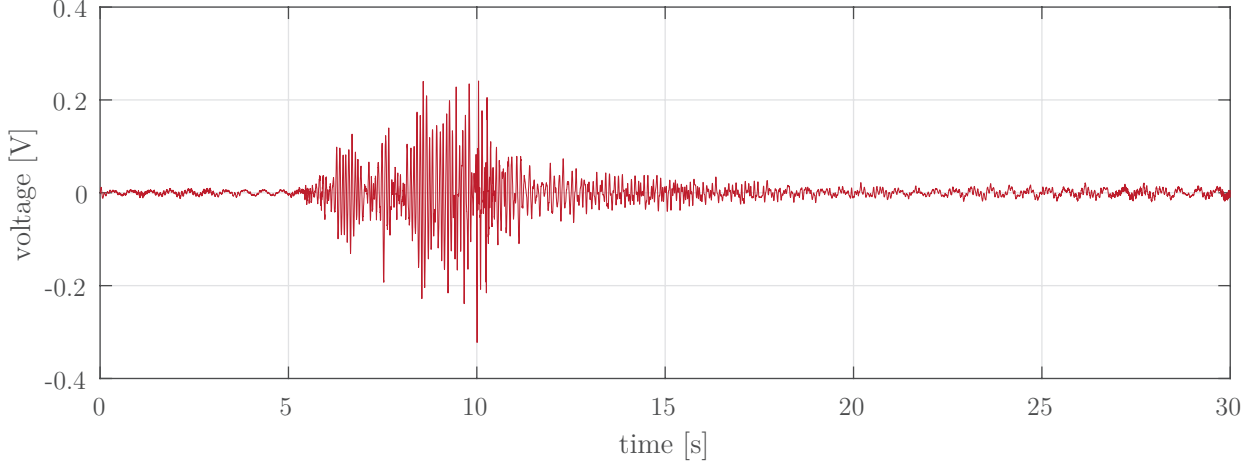


Figure 4: Estimated voltage signal for the event presented in figure 2, using a MOR model with 30 modes ($K = 30$).

3.2. Proposed Framework for the Optimisation

After the identification of the events, it is possible to apply the proposed optimisation procedure. The procedure consists in four major parts: (1) the optimisation of the PEH for each event, (2) the estimation of the optimal energy harvested for each event, (3) the clustering of optimal geometries, and (4) the estimation of the energy harvester for long time windows. The scheme of the procedure is shown in figure 6, where the steps are detailed next.

In **step 1**, shape optimisation is performed for each event (we call it Individual Event Optimisation) to identify the key resonance frequencies and limit the search space. Shape optimisation is performed for a representative number of events on the bridge (denoted by N_e). The optimisation for a single event is formalised as

$$\mathbf{x}^* = \arg \max_{\mathbf{x} \in \mathbf{X}} |E(\mathbf{x}|e)| \quad (25)$$

The objective function $E(\mathbf{x}|e)$ is the energy harvested from a specific event e by a PEH whose geometry is defined by vector \mathbf{x} . The optimisation is established to obtain the geometrical parameters to maximise $E(\mathbf{x}|e)$. The optimal design is denoted by \mathbf{x}^* . The optimal design for each event are schematically shown in Figure 6 assuming two design variables $\{x_1, x_2\}$ (Step 1). The objective function could be modified, for example to design PEHs considering the energy per unit of area or other. Particle Swarm Optimisation (PSO) [20, 21, 22] is the selected optimisation method due to its adequate performance for non-convex problems. In simple words, PSO is an iterative method where a population of candidate solutions (or particles) moves in the search space towards the best solution. Each particle has associated a position and a velocity, which are redefined in each iteration based on the individual and collective experience. The PSO method is expected to be an efficient optimization algorithm being fast and computationally cheap, also it can be parallelised increasing even more the computational efficiency.

Step 2 consists in computing the energy harvested by each optimal device \mathbf{x}^* , obtained in step 1, from all events, i.e.

$$E(\mathbf{x}^*) = \sum_{i=1}^{N_e} E(\mathbf{x}^*|e_i) \quad (26)$$

The energy harvested is estimated using equation 26 and the numerical integration of the power signal defined in the Eq. 24. In Figure 6 (Step 2), optimal designs are shown together with the corresponding $E(\mathbf{x}^*)$, represented by circles of proportionally varying radii. The calculation of the

Table 3: Substructure and Piezoelectric mechanical and electromechanical properties of the PEH used in the experimental validation

Model Parameters		
Substructure Density (ρ_s)	7725.7	[kg m ⁻³]
substructure Young Module (Y_s)	61.9	[GPa]
Compliance at constant electric field (s_{11}^E)	15.2	[pN ⁻¹ m ⁻²]
Piezoelectric Strain Constant (d_{31})	292.8	[pC N ⁻¹]
Permittivity at Constant Stress ($\varepsilon_{33}^T/\varepsilon_o$)	10299.1	[F m ⁻¹]
Piezoelectric Density(ρ_p)	7567.9	[kg m ⁻³]
Length (L)	23.9	[mm]
Width(W)	10.3	[mm]
Piezoelectric Thickness (h_p)	0.245	[mm]
Substructure Thickness (h_s)	0.232	[mm]
Damping Ratio (ζ)	0.0126	
$\varepsilon_o = 8.854 \times 10^{-12}$		

energy harvested from the database of each optimal geometry allows for improving the clustering performance in the next stage.

Step 3 consists in the Clustering and Candidate Identification. The optimal geometries from each event tend to have a natural frequency close to one of the bridge’s resonance frequencies. Thus, it is possible to group them in clusters based on the geometrical parameters (design variables) and the energy harvested from the events database. In Figure 6 (Step 3), optimal designs are schematically grouped into three clusters, denoted by yellow, red and green colours with their centroids denoted by black crosses. In this work, k -means [23, 24] is selected to cluster the geometries due to its ease of implementation, efficiency, empirical success, and adaptability in clusters of different shapes and sizes. k -means is an unsupervised machine learning algorithm that assigns each *point* (optimal design) in one k group based on its characteristics (geometric parameters and harvested energy from event data). The clusters are represented by a centroid which features are adjusted iteratively, minimising the distance with the assigned elements in the group. The number of clusters k needs to be set before starting the algorithm, however, an arbitrary selection does not guarantee the best clustering result. To deal with this issue, the Silhouette Method [25] is also included in this framework to find the optimal k value. The Silhouette method computes coefficients that measure how much a *point* is similar to its cluster compared to others, providing a metric to evaluate how well each object has been classified. Finally, once the optimal designs have been grouped, the centroids calculated from the k -means are defined as candidates to be the optimal PEH for continuous energy generation.

The last step, **Step 4**, consists in assessing the Energy Harvested from a 24-hour acceleration signal (or any other time window) for each candidate obtained in Step 3. The purpose of this step is to select the best option (among the candidates) for continuous energy generation. In the real life scenario, this is the preferred design because the device should generate the optimal amount of energy independently on the traffic on the bridge. In Figure 6 (Step 4), energy generated by three candidates (centroids identified in Figure 6 (Step 3)) is shown schematically.

The procedure proposed here, to optimise PEHs based on events (non-harmonic time series), is

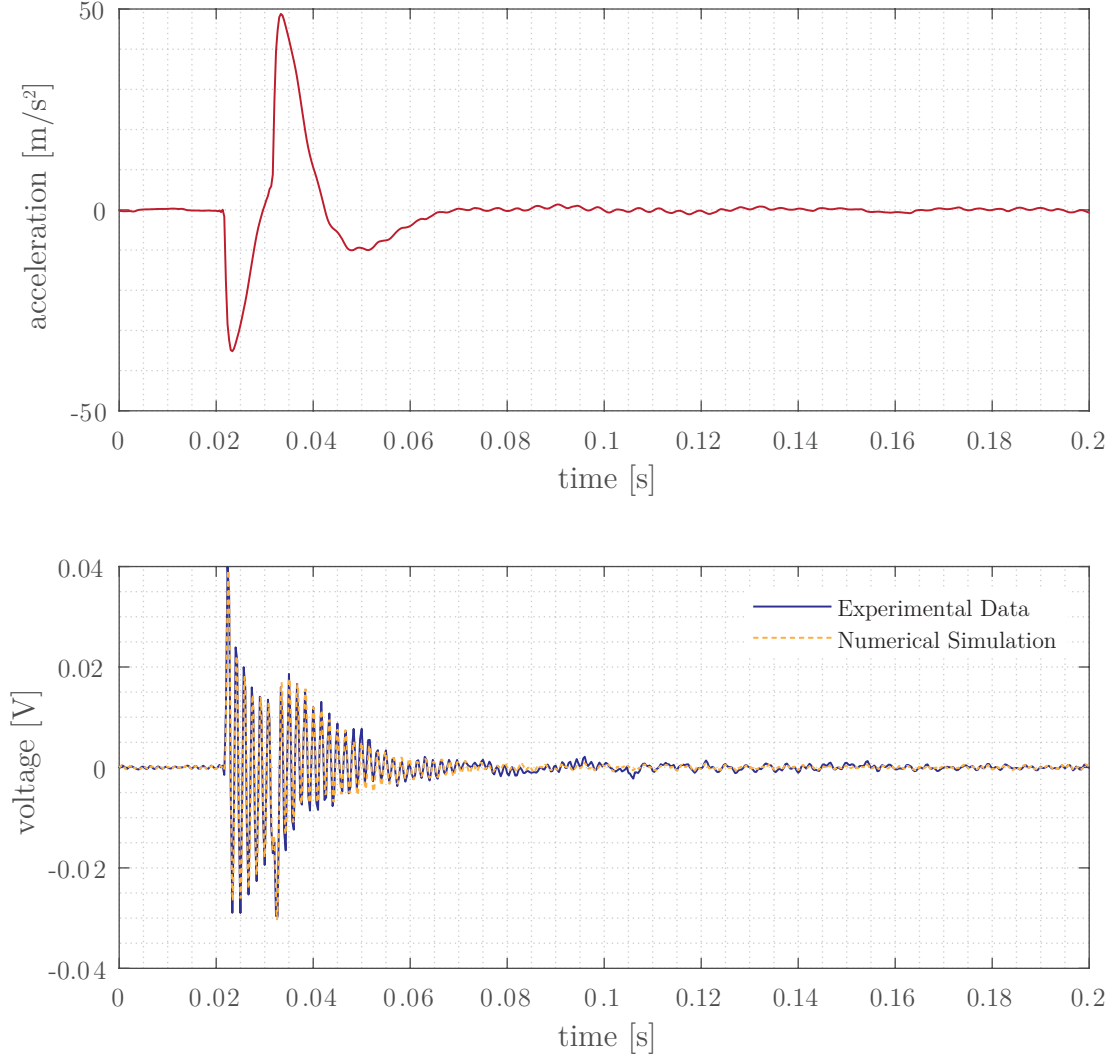


Figure 5: Experimental validation of the numerical model of the PEH. Top figure presents the experimental acceleration at the base of the PEH. Bottom figure compares the numerical prediction and the experimental voltage signals.

implemented later in the case study presented in Section 5 for an in service bridge. But first, and for the sake of comparison, Section 4 presents another case study where a PEH is optimise adopting a harmonic excitation.

4. Case Study 1: Optimization of PEHs for Bridges Assuming Harmonic Excitations

In this section, a comprehensible study is carried out to understand how the piezoelectric device's design impacts the energy harvesting in bridges. First, the effect of the damping on different geometries is discussed. Second, a procedure to select the electrical resistance is presented. Next, a parametric study is performed to understand the effect of the geometric parameters on the voltage generation considering harmonic accelerations. Finally, an optimisation problem to maximise the energy harvesting from a bridge is formulated and solved. The optimal results are compared with the parametric study. This case study serves as a benchmark problem to be compared with the procedure proposed in Section 3, this comparison is presented later in Section 5.

Five parameters define the geometry of the harvester: the total length L , the aspect ratio $R = W/L$ (relation between the width W and the total length L), dimensionless piezoelectric length $l = L_{pzt}/L$

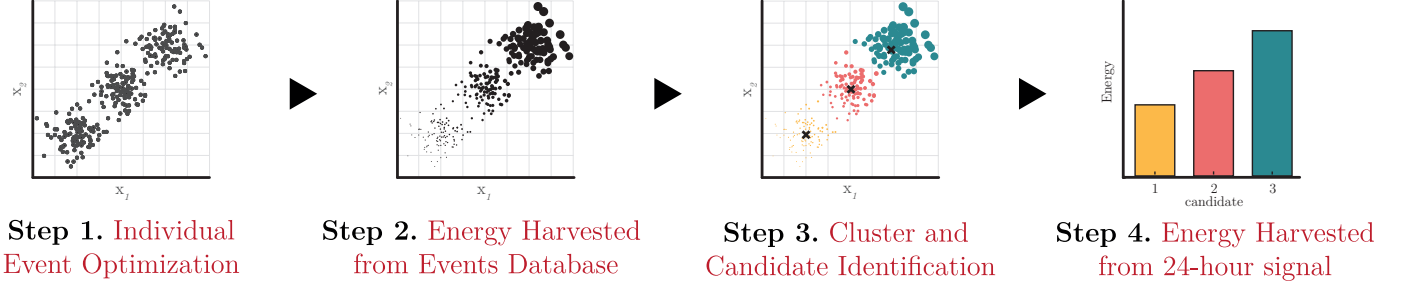


Figure 6: Overview of the proposed optimization framework.

(relation between the length of the piezoelectric layers L_{pzt} and the total length L), the total thickness $h = h_s + 2h_p$, and the dimensionless piezoelectric thickness $H = h_p/h$ (relation between the thickness of a piezoelectric layer h_p and the total thickness h), please refers to Figure 1 for reference. A bronze substructure and two PZT 5A piezoceramic sheets connected in series are considered. The corresponding material properties are given in Table 2.

Three design scenarios for parameters (L, R, l, H) are carried out, all of them with $h = 1\text{mm}$. In each case, two parameters are fixed and two are considered as design variables:

- **Design 1:** $H = 0.25$, $l = 1$, the design variables are: $L \in [10, 50]$ cm and $R \in [0.3, 1]$
- **Design 2:** $R = 1$, $l = 1$, the design variables are: $L \in [10, 50]$ cm and $H \in [0.05, 0.45]$
- **Design 3:** $R = 1$, $H = 0.25$, the design variables are: $L \in [10, 50]$ cm and $l \in [0.1, 1]$

The motivation to keep only two design variables instead of four is to help the visualisation and facilitate the interpretation of the results.

4.1. Damping Effect

As it was mentioned in Section 2, it is adopted a proportional damping model, thus, the damping matrix is defined as $\mathbf{C} = \alpha\mathbf{M} + \beta\mathbf{K}$ where the value of α and β are considered invariant. The assumption of invariability of the constants has been used in previous works [13, 11, 12]. If the problem is presented in modal coordinates, the damping matrix is redefined according to equation (23) as $\mathbf{c}_o = \mathbf{m}_o^{-1}\mathbf{\Phi}_o^T\mathbf{C}\mathbf{\Phi}_o = \text{diag}(2\zeta_1\omega_1, \dots, 2\zeta_K\omega_K)$. In particular, the damping ratio is a good metric to describe the effect of changing shape. As the dominant vibration frequencies in bridges are low, it is common to design the PEH based on its first natural frequency. Hence, the most relevant damping ration of the PEH corresponds to ζ_1 .

Figure 7 shows the isocurves of the damping ratios ζ_1 (black lines) in three design scenarios: Design 1 (left) in plane (R, L) , Design 2 (middle) in plane (H, L) and Design 3 (right) in plane (l, L) . In all cases, the damping constants are $\alpha = 14.65$ rad/s and $\beta = 10^{-5}$ rad/s. In all three design scenarios, it is observed a strong dependence of ζ_1 on L , which is associated with the dependence of ζ_1 on the device's mass and stiffness. Additionally, both ζ_1 and the mass seem almost independent on the second parameter $(R, H$ or $l)$.

4.2. Electrical Resistance Selection

As it has been discussed in other works [13, 11, 26, 27], the choice of external electrical resistance, R_l , directly affects the energy harvesting of a piezoelectric device. Therefore, energy generation can be significantly increased by choosing an optimal value of R_l . As previously stated, it is convenient to increase the power in the first vibration mode since the bridge frequencies are low. Then, the electrical

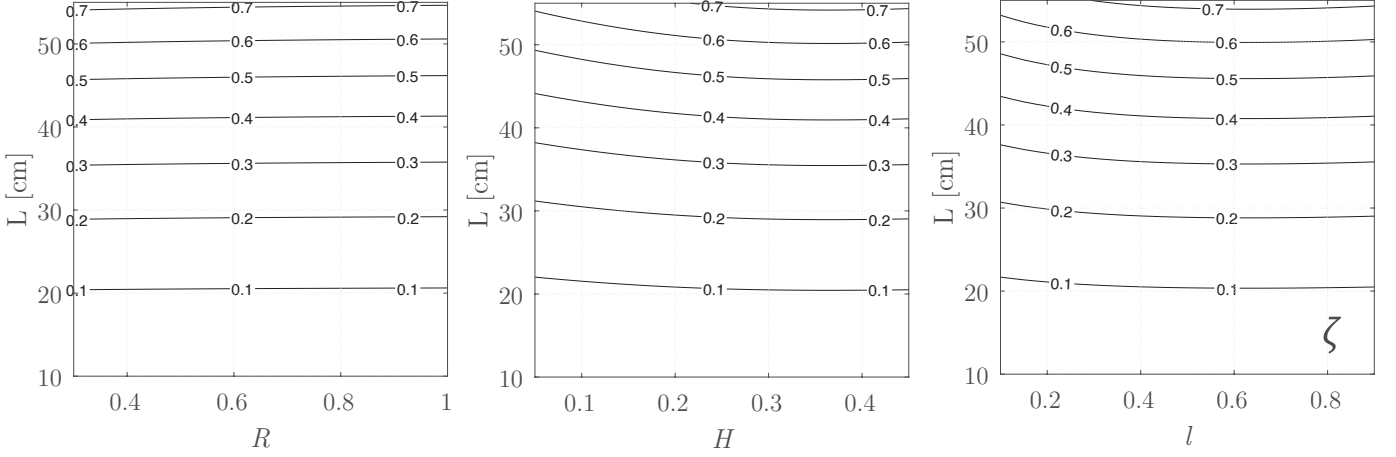


Figure 7: Isocurves for damping ratios ζ_1 for the geometries in the three design scenarios: Design 1 (left), Design 2 (middle), Design 3 (right). The proportional damping coefficients correspond to $\alpha = 14.65$ rad/s and $\beta = 10^{-5}$ rad/s.

resistance R_l^* can be chosen to maximise the value of the power FRF at the first resonance frequency ω_o . Note that ω_o is defined here as the frequency in which the power FRF has its maximum, thus, ω_o is expected to be close to the undamped frequency ω_1 . Such optimisation problem can be expressed as

$$R_l^* = \arg \max_{R_l \in \mathbf{R}_l} |H_p(\omega_o, R_l | \mathbf{x})| \quad (27)$$

with

$$H_p(\cdot) = \frac{H_v(\cdot)^2}{R_l} \quad (28)$$

where $H_v(\cdot)$ is the voltage FRF defined in the equation (16), and the vector \mathbf{x} defines the device geometry ($\mathbf{x} = [L \ R]$ for Design 1, $\mathbf{x} = [L \ H]$ for Design 2, and $\mathbf{x} = [L \ l]$ for Design 3). Note that the power FRF is evaluated at the first resonance frequency ω_o . However, ω_o depends on the value of the external electrical resistance R_l , then ω_o can be considered as a function of R_l . Therefore, the value of $H_p(\omega_o(\bar{R}_l), \bar{R}_l | \mathbf{x})$ is calculated numerically and the optimisation problem, equation (27), is solved using the Nelder-Mead Simplex Method [28] (implemented in Matlab function **fminsearch**).

Figure 8 shows the selected optimal values of the electrical resistance R_l^* for the three studied designs. In general, the optimal resistance is almost independent on L for values higher than 30 cm. For the other variables, there is a strong dependence on the optimal value R_l^* . The results show the importance of properly choosing the external resistance. The procedure to select the external electrical resistance will be used in the subsequent studies to increase power generation.

4.3. Optimization based on Harmonic Excitations

A parametric study is carried out for the three design scenarios defined above. The electrical resistance adopted is optimal and selected following the procedure proposed in the previous section. The results are shown in Figure 9, where the effect of the size, shape and distribution of the piezo-electric material on the natural frequency ω_o and its respective power H_o are studied. The isocurves for ω_o and H_o in the (R, L) plane for Design 1 are represented in Figure 9a with a red and black line, respectively. As expected, ω_o decreases with increasing length L due to the reduction in stiffness and the increase in mass. On the other hand, ω_o is almost independent of R . Concerning the maximum power H_o , the increase of R and L favours the generation of energy due to the increase in the device area and the amount of mass that increases the inertial effect.

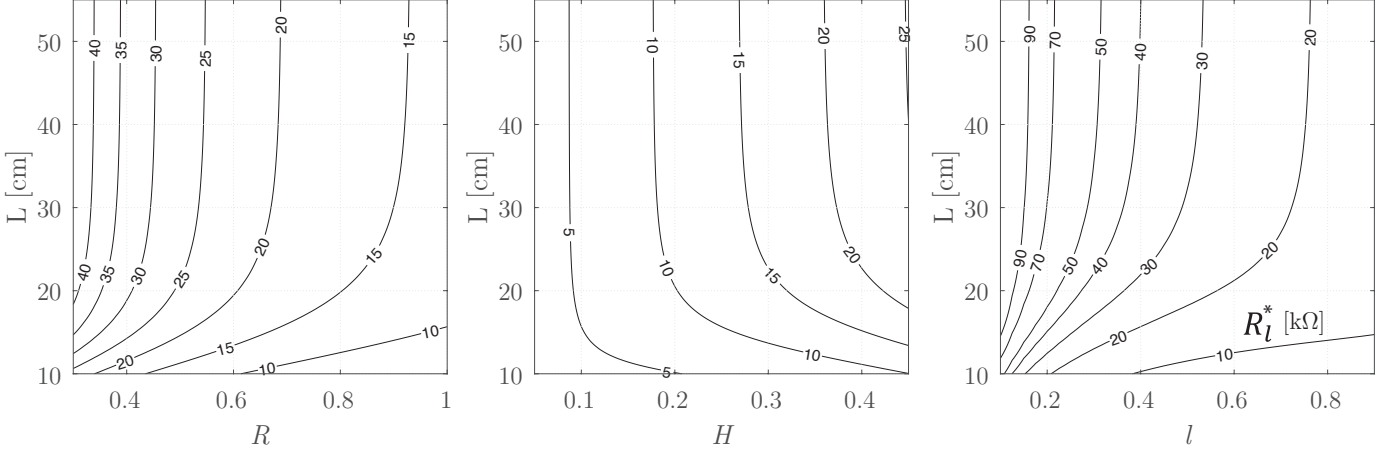


Figure 8: Isocurves for external optimal electrical resistances R_l^* that maximise power generation at the fundamental frequency for the geometries in the three study cases: case 1 (left), case 2 (middle) and case 3 (right).

Figure 9b shows the ω_o (red line) and H_o (black line) isocurves in the (H, L) plane for fully covered square devices (Design 2). Note that when the dimensionless thickness H is increased for any L , a slight increase in the natural frequency ω_o is observed. It must be taken into account that the piezoelectric material has a lower density and Young's modulus than the substructure. This implies that the mass and stiffness of the device decrease when H increases. However, the change in stiffness is the one that dominates the dynamic behaviour producing a decrement in ω_o . Regarding the generated power H_o , it increases with L mainly due to the increase in the PZT area. On the other hand, there is an increment and subsequently a reduction of H_o with increasing H . This behaviour is the result of different factors. First, increasing the thickness of the piezoelectric layer decreases the inertial effect of the structure and consequently, there is less mechanical forcing over the PEH. Furthermore, the electromechanical coupling and the capacitance of the device are inversely proportional to the thickness h_p . In addition, a higher value of H brings an increment in the flexibility of the device, which favours the increment in deformations during the excitation.

The isocurves of ω_o and H_o in the (l, L) plane for Design 3 are shown in Figure 9c. As seen in the Figure, the natural frequency slightly increases when l decreases. In this case, the increase in inertia in the area of the device's tip dominates the behaviour and produces the variation as mentioned earlier of ω_o . On the other hand, similar to the previous cases, the natural frequency is proportional to L despite increasing damping ratios. Regarding H_o , it increases and then decreases as l decreases. It is due to the increase in the excitation force related to the greater inertia of the device. However, the decrease in l implies a decrease in the area of the piezoelectric layers, responsible for the subsequent decrease in power H_o .

From these parametric studies it is possible to identify geometries that maximise the generated power H_o for different natural frequencies ω_o (this is done by finding the intersection of the ω_o -isoline with the H_o -isoline with highest value of H_o). These intersection points form lines, which are colored in grey and shown in Figure 9. Note that these results are independent of the bridge. Then, the designer can take the dominant vibration frequency of a particular bridge and select the geometry of the PEH based on the grey lines shown in figure 9.

This parametric study reveals the importance of properly selecting the geometry of the PEH in order to maximise power output. However, the results presented in Figure 9 are obtained adopting a single harmonic loading, i.e. $a_b = A_b e^{i\omega t}$. Hence, it is of interest to compare these results when a realistic excitation is applied over the PEH. This issue is addressed in the following case study.

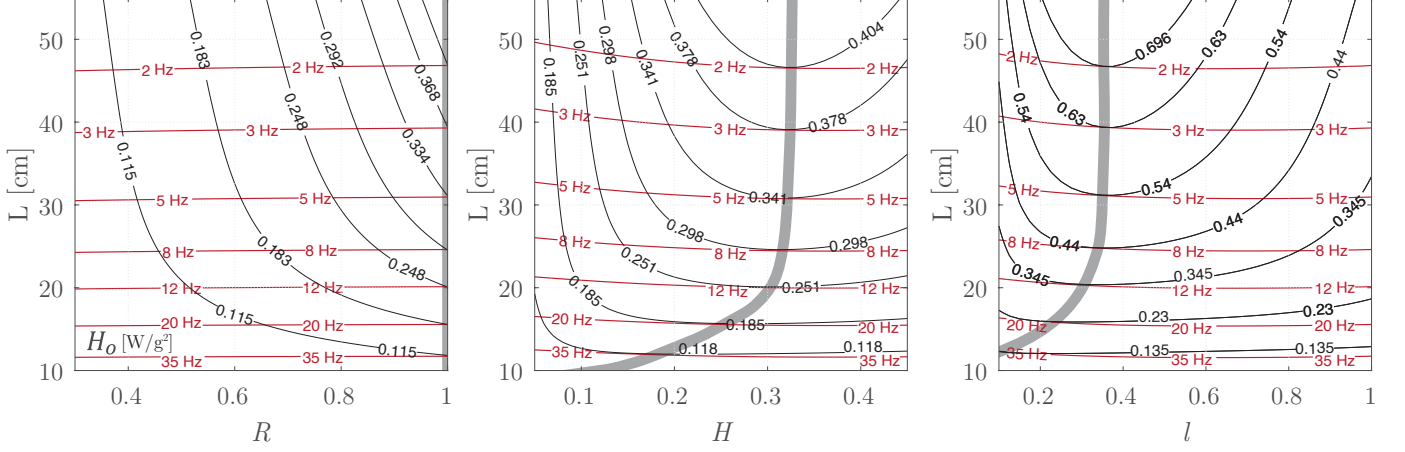


Figure 9: Isocurves for peak amplitude H_o of power FRF (black lines) and isocurves for natural frequencies ω_o (red lines) for the three design scenarios studied. The grey line corresponds to optimal geometries for any given natural frequency ω_o .

5. Case Study 2: Optimization of PEHs for an in service Bridge Using Time Series Excitations

A cable-stayed bridge, shown in Figure 10, carrying one traffic lane and one pedestrian lane with a maximum loading capacity of 30 tons over the Great Western Highway in the state of New South Wales (NSW), Australia, was analysed in [29], and it is chosen as a case study in this work. The structural system consists of a composite steel-concrete deck spanning over 46.2m and an A-shaped steel pylon with a height of 33m. The width and the depth of the concrete deck are uniform at 6.30m and 0.16m, respectively. The deck is supported by four longitudinal girders which are internally attached by a set of seven cross girders (CGs), see Figure 11. Sixteen semi-fan arranged pre-tensioned stayed-cables with a diameter of 38mm are anchored on steel tower and cross girders.

A dense array of timely-synchronised sensors, including strain gauges and accelerometers have been installed on the bridge since 2016 [30]. Twenty-four uni-axial accelerometer sensors were permanently placed under the deck at the intersection of the girders and floor beams to measure the vertical acceleration of the bridge, see Figure 11. These sensors are low-noise capacitive accelerometers [2210-002 Silicon Design] which can detect acceleration within the range of $\pm 2g$ with a sensitivity of 2,000 mV/g. The signal conditioning and data logging software consist of an embedded PC and HBM Quantum-X data logger to record data. This system provides an integrated and reliable device to log high-quality data with 24-bit resolution with bandwidth capability of 0–3 kHz. All data are collected at a default sample rate of 600 Hz with an anti-aliasing filter. The 3-dB cutoff frequency of the filter is 100 Hz and it is a fourth-order Bessel low-pass filter.

Following the procedure proposed in Section 3.1. 1000 events were extracted in a period of seven days and were numerically labeled in order of appearance. The acceleration threshold to define the event was set in 0.15 m/s^2 . The events can be caused by environmental conditions or by the passage of vehicles over the bridge. Acceleration measured at sensor A14 was chosen for this study due to its location at the center of the bridge. Based on the conclusions of some previous studies [7, 10], the PEH performance for such location is expected to be higher. The event labeled as 2 was already presented in Figure 2. All events are confined by a time window of 30s where its peak acceleration occurs at the time of 10s.

Although the bridge has only one traffic line, the vehicles can transit in both directions because



Figure 10: Illustration of the cable-stayed bridge located in the state of NSW, Australia.

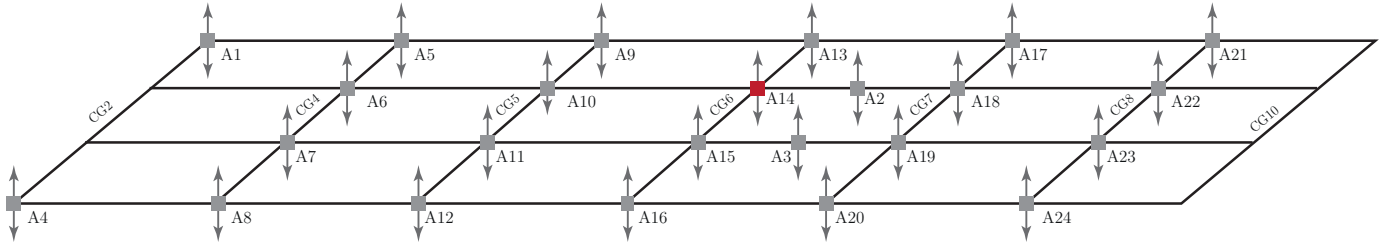


Figure 11: Illustration of the sensor layout under the deck.

the traffic flow is not high. Also, the first natural frequencies are low, i.e., 2 and 3.5 Hz. These bridge features could condition the performance of the piezoelectric devices.

5.1. Optimisation based on Harmonic Excitation versus based on Time Series

This section presents a comparison between the benchmark problem presented in case study 1 (optimization of PEHs based on harmonic excitations) and the optimal geometries identified by imposing excitations directly recorded from the bridge of study. For the sake of comparison, the design scenarios are the same of case study 1 but this time the optimisation is performed using 1000 events following the procedure presented in Step 1 of the proposed framework (please refers to 3.2).

The optimisation for each event is based on the PSO method employing thirty particles. Figure 12 presents the iso-curves of the energy harvested from event 2 for the three design scenarios. In addition, the optimal geometries are marked with a star in the three figures. It is observed that the optimal geometry, obtained by the PSO, corresponds to the position estimated by the isocurves, which demonstrates the method converges to a correct value (global maximum). Convergence of the objective function is shown in Figure 13. The figure shows that twenty iterations are enough to find the optimal value.

Figure 14 shows the 1000 optimal PEH designs (one for each event) marked with blue, yellow and red dots for Design 1, 2 and 3, respectively. Additionally, the figure shows the isocurve of the natural frequencies for different geometries (red line) and optimal designs using harmonic excitations (grey

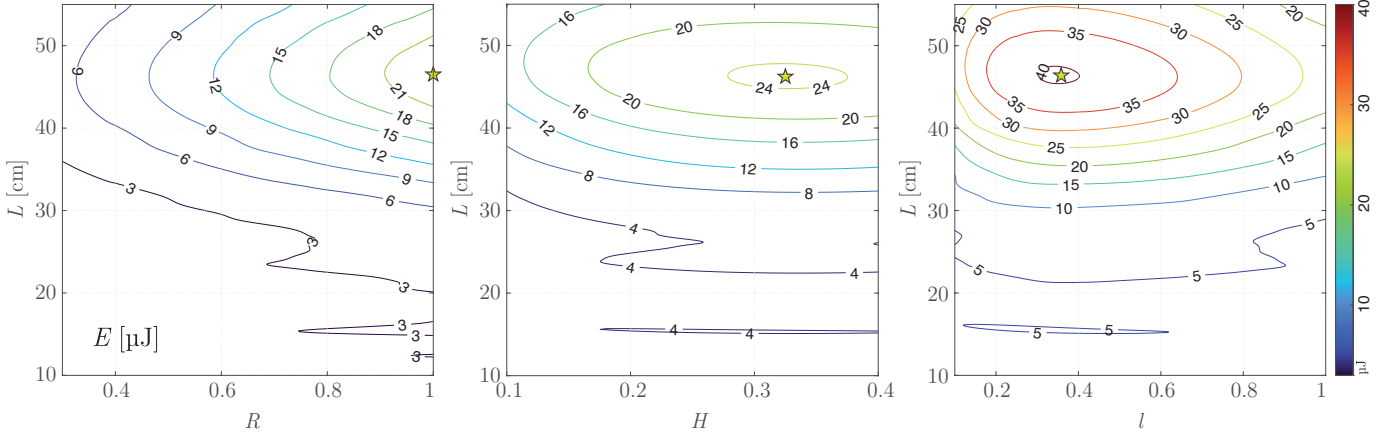


Figure 12: Isocurves for harvested energy from event 2 and the optimal geometry obtained from the PSO method: Design 1 (left), Design 2 (middle), Design 3 (right).

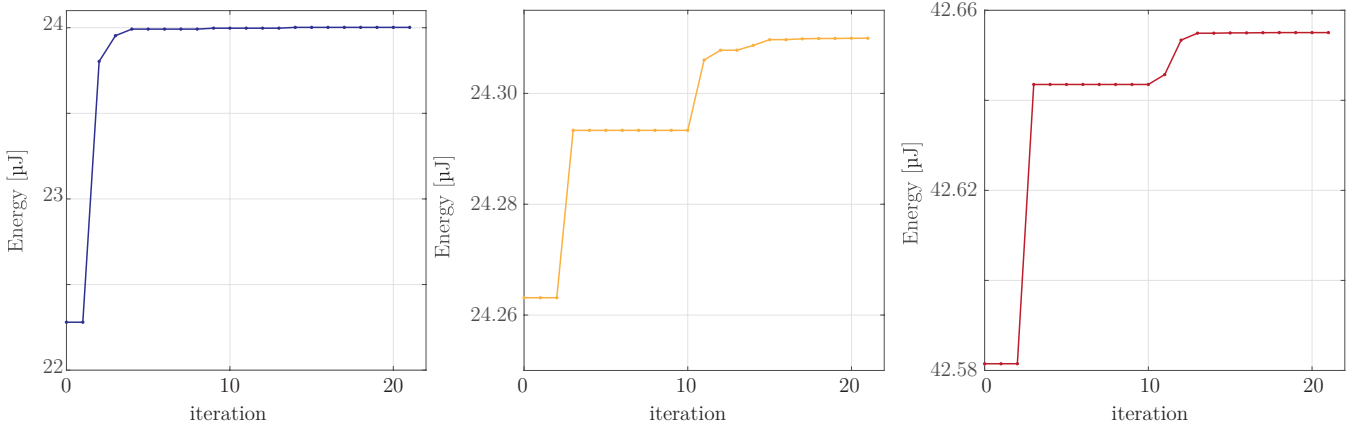


Figure 13: Optimal objective function in each iteration: Design 1 (left), Design 2 (middle), Design 3 (right).

area) identified in the benchmark problem (Case Study 1). The results show that for Design 1 and 2, the optimal geometries (blue and yellow dots) are aligned along the grey line, as expected. However, in Design 3, red dots show significant deviations from the grey line. These dispersions are explained by the discrepancies in predominant frequencies among the events as it is discuss next.

To study the relationship between the dynamic characteristics of the device and the event frequency spectrum, Figure 15 presents the comparison of FRFs of six optimal designs and the Fourier acceleration spectrum of their respective event for the three design scenarios. Six optimal designs are identified in Figure 14 with the purpose to be compared, which correspond to events 2, 113, 304, 384, 781 and 718. First, note that the fundamental frequency of the piezoelectric devices is tuned with the predominant frequency of the acceleration spectrum. However, the acceleration peak is not always the one with the highest amplitude, such as the events 781 and 718 where the devices' fundamental frequency is tuned with the widest acceleration spectrum peak. Also, it is important to mention that there is consistency between the optimal FRFs for the three design scenarios, since the fundamental frequencies coincide in the six studied events.

Note that optimal designs within the grey line are those who generate the higher energy from their first vibration mode. This is valid for all PEHs in Designs 1 and 2. In this sense, there is consistency in these results, meaning that, by grouping the optimal designs around some key frequency, the corresponding events share frequency characteristics. Figure 16 presents the Fourier spectra of the

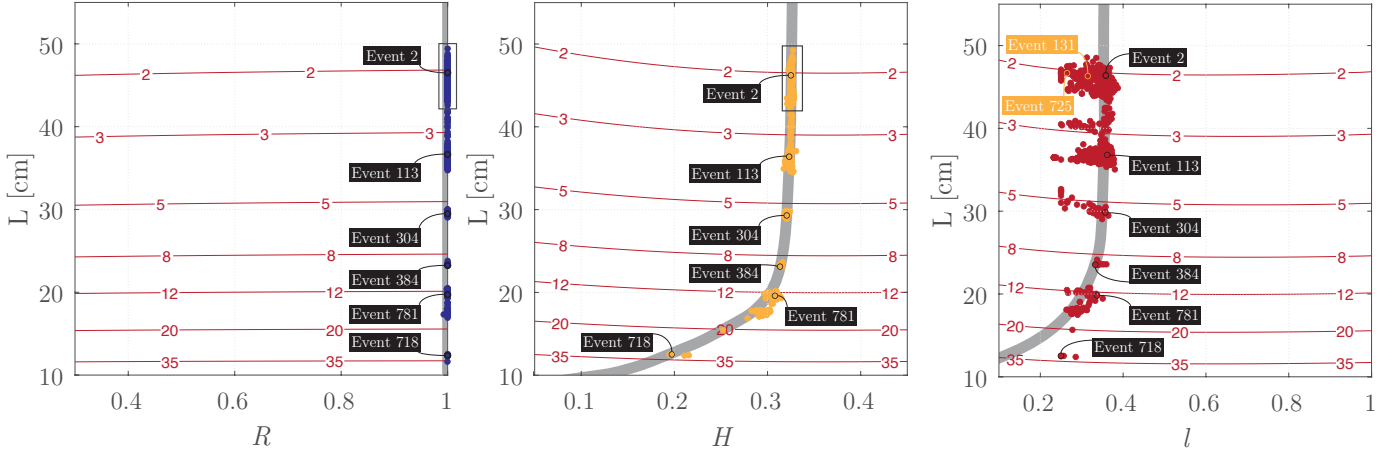


Figure 14: Isocurves for fundamental frequencies ω_o (red lines). (a) Optimal geometries for the 1000 Events in Design 1 (blue dots). (b) Optimal geometries for the 1000 Events in Design 2 (yellow dots). (c) Optimal geometries for the 1000 Events in Design 3 (red dots). The geometries related to events 2, 113, 304, 384, 781 and 718 are identified in three figures; also geometries for events 113 and 728 are denoted in the right figure. The geometries around the 2 Hz are marked by a rectangle in the left and central figures.

events associated with PEH design around the 2 Hz, which are identified by a rectangle in Figure 14-a and 14-b. As expected, it is seen that the predominated frequency is around 2 Hz, the same as the natural frequency of the optimal harvesters.

To understand the higher dispersion of the optimal geometries for Design 3, Figure 17 presents the comparison between the FRFs of three optimal designs and the Fourier acceleration spectrum of their respective event. The three optimal designs are identified in Figure 14-c, which correspond to events 2, 131 and 725. The three devices have the first natural frequency of 2Hz. The high dispersion is explained by analysing the second natural frequency of the FRF. The main difference between Designs 1 and 2, and Design 3 is in the second natural frequency, which is more sensitive to change in parameter l rather than parameters R or H . The change in parameter l allows increasing the energy generation from the second mode of vibration, slightly decreasing the energy generation from the first one, leading to a higher energy overall. Therefore, the main conclusion from this study is that according to the spectral characteristics of an event, in some cases it is better to use devices that harvest energy only around the first natural frequency, while in others it is more efficient to harvest energy simultaneously from the first two natural frequencies. Despite the fact that it might reduce the energy generation in the first range in order to favour energy generation in the second.

The results of this section can be summarised as follows. The optimisation problem using the event acceleration response in the bridge yields the results, expected from the FRF analysis and parametric studies. Obtained results are consistent among the studied cases. It was found that not always the best option is to tune and maximise the energy generation in one frequency (prediction areas). Also, the natural frequency of the optimal device is not always close to the highest peak of the acceleration spectrum of the corresponding event. All these issues are considered by the direct optimisation of the events in the time domain, giving it greater robustness than the design obtained by simply tuning the natural frequency of the device with a target value. Nevertheless, the optimal designs from different events present a high dispersion in case 3, where one of the design parameters is the ratio between the PZT-layer length and the overall device length, which makes the design sensitive with respect to the second fundamental frequency. In practice, we are interested in designing one or a limited number of piezoelectric devices for a continuous generation; thus, it is not feasible to design a device for each

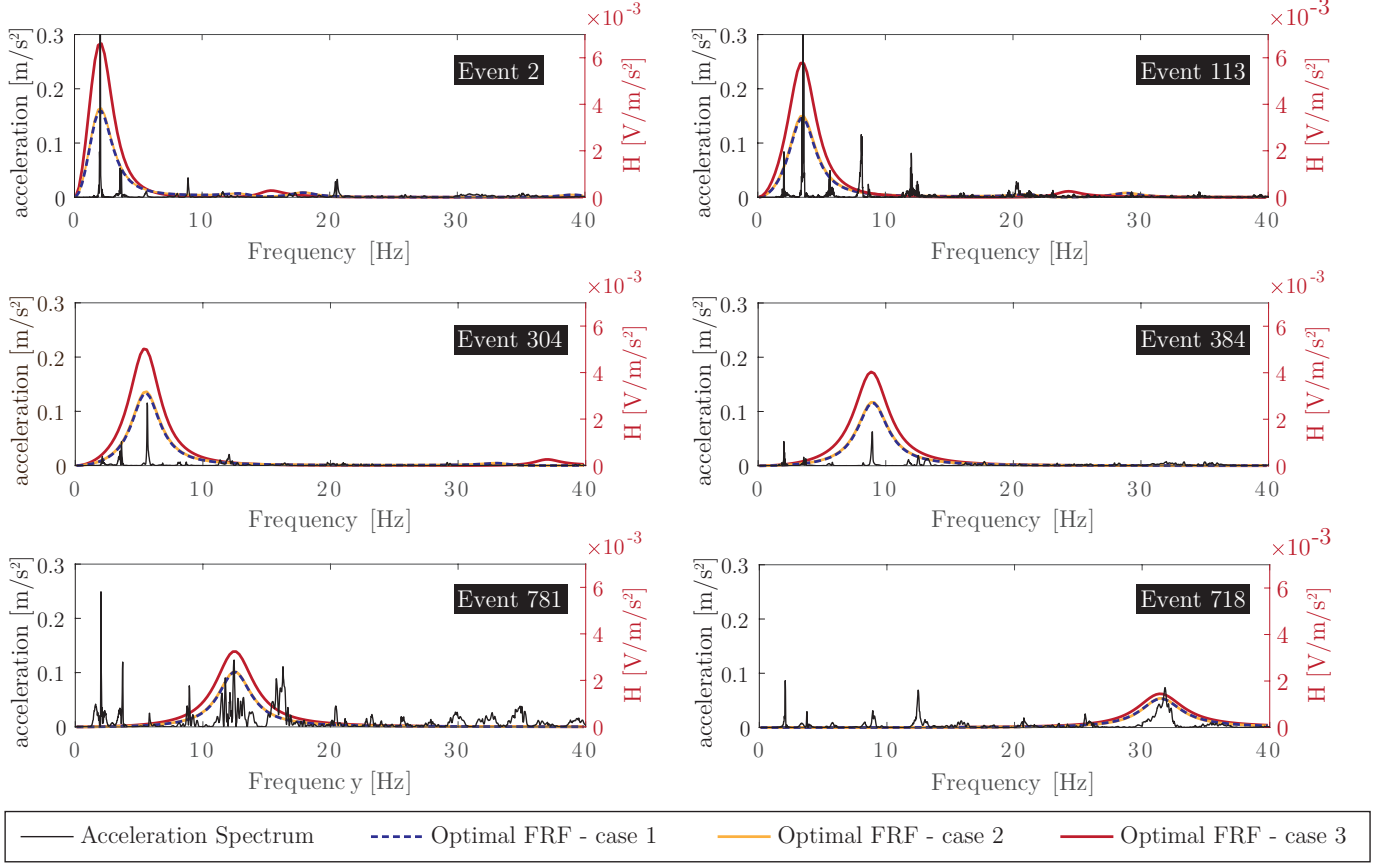


Figure 15: Comparison between the Fourier spectrum of the event acceleration signal and the FRFs of the optimal geometries obtained from the three design scenarios for events 2, 113, 304, 384, 781 and 718.

event or perform an optimisation process in long time windows due to computational limitations. In that sense, the next section will present an optimisation framework for designing piezoelectric devices for a continuous generation based on the results presented in this section.

5.2. Optimisation based on Time Series for a Time Window of 24hrs

The optimisation framework proposed in Section 3 is applied to the cable-stayed bridge presented here. The framework is expected to offer candidates to maximise the energy harvested in continuous operation. 1000 Events are considered in this case as a representative number for this bridge because it is the approximate number of events that occur during a week even though the selected events are drawn from different periods. The PEH materials are chosen the same as in section 4. A serial connection between the piezoelectric layers is considered, and the selected electrical resistance for each geometry is the one that maximises the peak of the FRF at the fundamental frequency. Five design parameters describe the geometry: total length $L \in [10, 50]$ cm, aspect ratio $R \in [0.3, 1]$, dimensionless piezoelectric length $l \in [0.1, 1]$, dimensionless piezoelectric thickness $H \in [0.05, 0.45]$, and total thickness h which is assumed constant and equal to 1 mm. Design variables are defined as

$$\mathbf{x} = \{R, L, l, H\} \quad (29)$$

First, the individual event optimisation was performed for 1000 events. As a result, 1000 optimal geometries were obtained. It was observed that all optimal geometries correspond to $R = 1$, which is in agreement with the results in section 4.3, hence variable R is omitted from the further analysis.

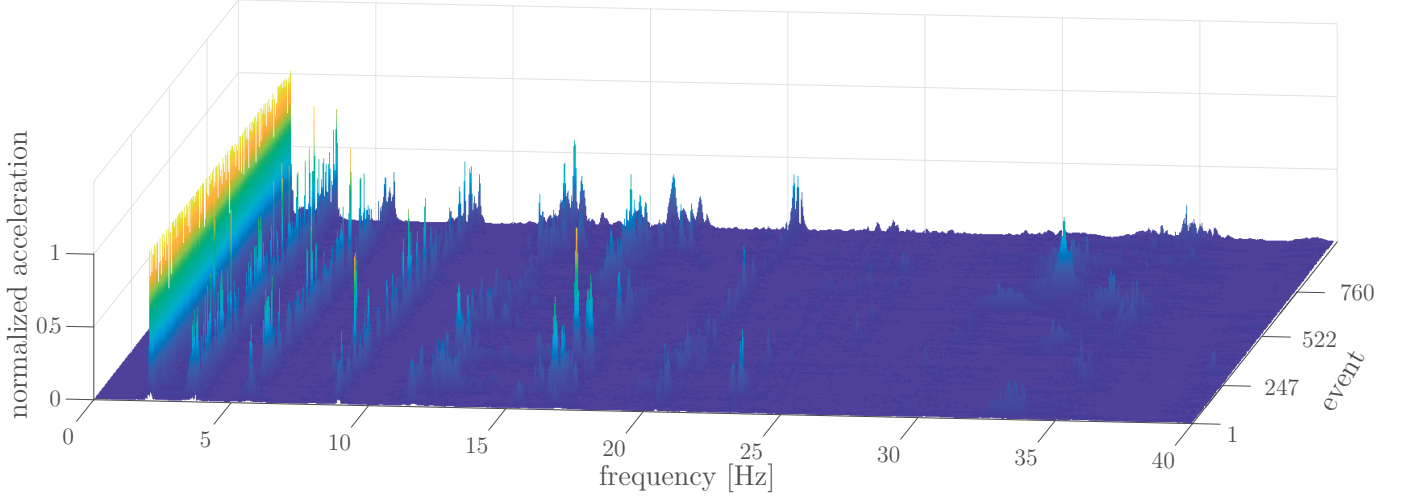


Figure 16: Comparison of the normalised Fourier spectra of event acceleration signal around 2 Hz in Designs 1 and 2.

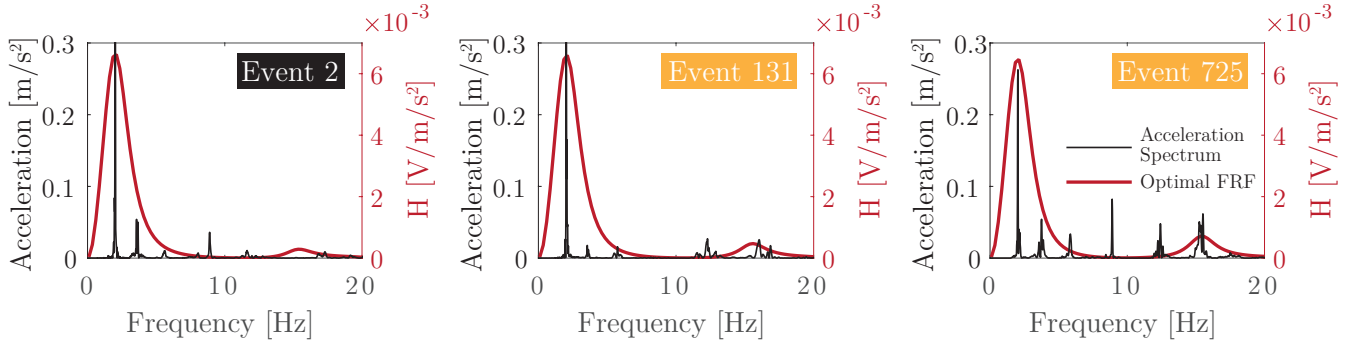


Figure 17: Comparison between the Fourier spectrum of event acceleration signal and the FRFs of the optimal geometries from the three shape optimisation cases for events 2, 131 and 725.

Optimal designs are shown in Figure 18 in $L - l - H$ space and their projections in the $L - l$ and $L - H$ planes. From Figure 18b it can be seen that the results present a high dispersion in the variable L and low in the variable H . The high dispersion in L is explained by its strong dependence with the natural frequency of the device, the high variability in the predominant frequencies between the events, and the fact that the devices tend to sync to the event's predominant frequencies. In Figure 18c, it is possible to observe a dispersion in the variable l . This is explained by the fact that the devices tune their first two resonance frequencies with some bridge's natural frequencies in some events. In particular, l allows increasing the energy generation from the second mode of vibration, slightly decreasing the energy generation from the first one, leading to an overall higher harvested energy according to the specific spectral characteristic of the event.

After the individual event optimisation, the amount of energy that each optimal design harvests from all events is quantified, which will be used to improve the clustering performance in the next step. Figure 19 shows the results, where the size of the indicator points of each optimal geometry is proportional to the energy harvested from all events. The results are presented in the $L - l - H$ space and their projection in the $L - l$ and $L - H$ planes. From Figure 19 one can notice that the most significant amount of energy is generated by devices with a length L around 45 cm, whose fundamental frequency is close to 2 Hz. This gives us a first estimate of the best candidates for the energy generation from a continuous 24 hour signal. However, this analysis does not consider the occurrence of similar events between them.

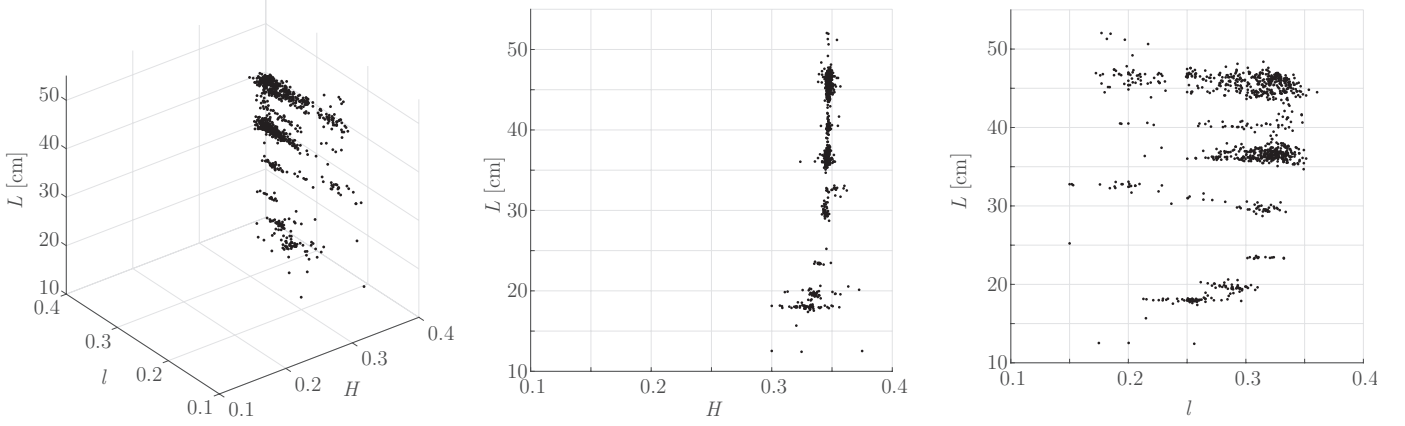


Figure 18: Optimal geometries for 1000 Events in the $L-l-H$ space (left), $L-H$ plane (middle) and $L-l$ plane (right).

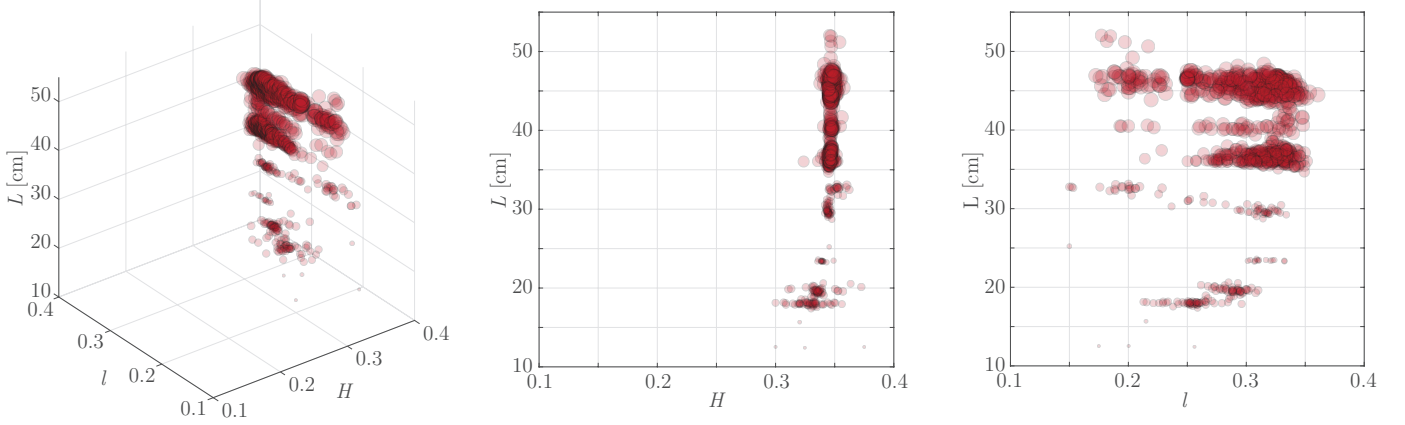


Figure 19: Energy harvested by the 1000 optimal devices from the full event database in the $L-l-H$ space (left), $L-H$ plane (middle) and $L-l$ plane (right).

After the energy quantification, cluster identification is carried out where the optimal geometries are grouped based on the similarity between them, taking into account the geometric variables L , l and H , in addition to the energy harvested from the full database. The cluster number is determined based on the Silhouette coefficient, which allow evaluating how well each geometry has been classified in their cluster with respect to the others. The results for different cluster numbers are presented in Figure 20, where it is concluded that the optimal number is 6 clusters. Next, cluster identification is performed based on the k -means algorithm. The six clusters and their respective centroids are presented in Figure 21. In this framework, the centroids are considered to be representative candidates of each cluster. Finally, the 1000 optimal geometries have been reduced to six candidates that will be evaluated for the continuous power generation.

The cable stayed bridge studied in this work is generally not subjected to high traffic, so the frequency of occurrence of events is low. Therefore, the optimisation framework is also evaluated in time windows without events (i.e., small oscillations in response to environmental conditions) since this condition prevails over time. In addition, this analysis will function as a control group for the present case study. 100 time windows of 30 seconds without events are extracted from the same period considered in the 1000 event extraction. Then for each time window, the corresponding acceleration signal is used as an input in the optimisation problem. The results of such individual optimisation are

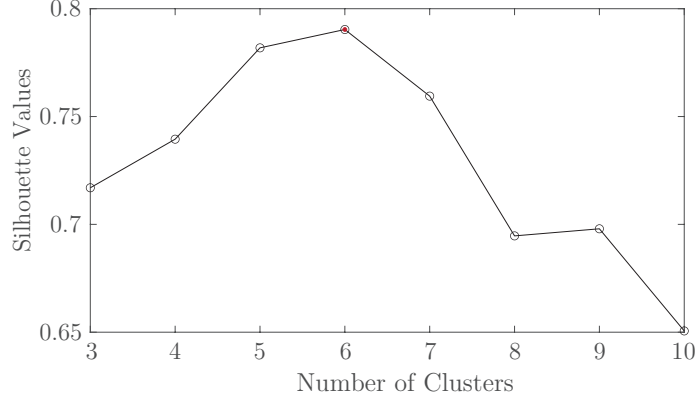


Figure 20: Silhouette Coefficient for different k -values applied to the 1000 optimal geometries.

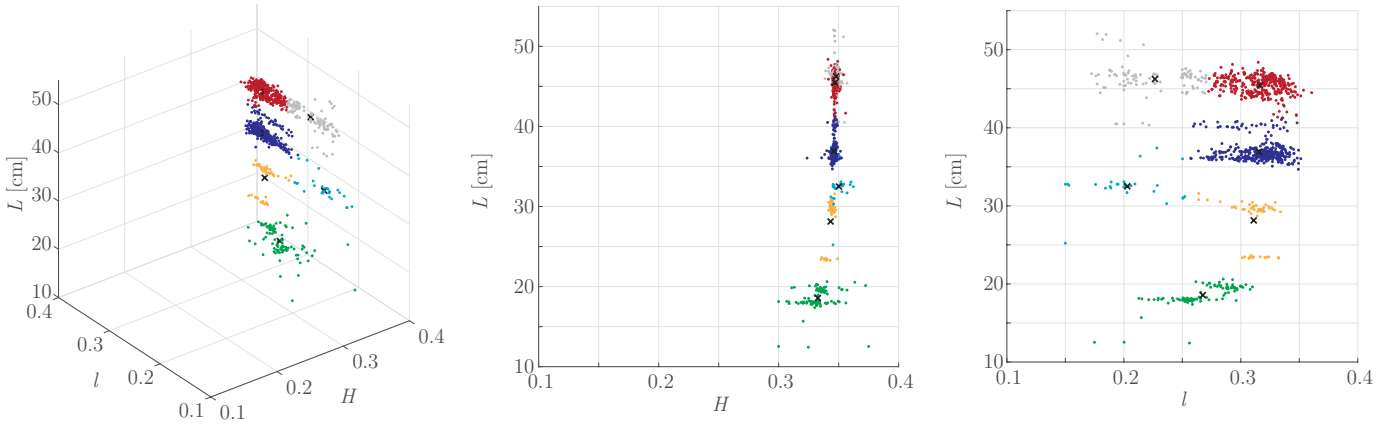


Figure 21: Six clusters of the optimal geometries for 1000 events in the $L - l - H$ space (left), $L - H$ plane (middle) and $L - l$ plane (right). Black crosses denote candidates (centroid of each cluster).

shown in Figure 22. Note that the optimal geometries present a low dispersion, as expected, since the oscillations in the absence of traffic are consistent in time. Therefore, it seems reasonable to consider only one design candidate to evaluate it in the continuous operation and compare it with the other six candidates defined above.

Finally, the seven PEH candidates are evaluated under 24 hour continuous operation conditions. Figure 23 presents their power FRFs, where it is possible to identify their natural frequencies. Note that these values coincide with the frequencies, where the optimal geometries from the optimisation in section 5.1 are grouped. It is also important to note that the first two natural frequencies of candidates 1 and 2 coincide and only vary in their amplitude in the FRF, which agrees with the results observed and discussed previously in Design 3 of section 5.1. Next, Figure 24 presents the energy harvested from a 24 hour signal by the seven candidates. We can conclude that the candidates with the highest performance are the candidates whose first natural frequency is around 2 Hz, with candidate 7 being the one that generates the most energy. Note that candidate 7 is representative of event-less window optimisations. However, the energy harvested by the best candidate is only 0.47% and 3.79% higher than candidates 1 and 2, respectively.

Although the optimisation framework suggests that the optimal device is the one obtained from the optimisation of the windows without events, this cannot be generalised to any bridge since it depends on different factors such as the structure of the bridge, the vehicular characteristics and the frequency of the traffic, all of them impacting the event's occurrence rate. The factors mentioned

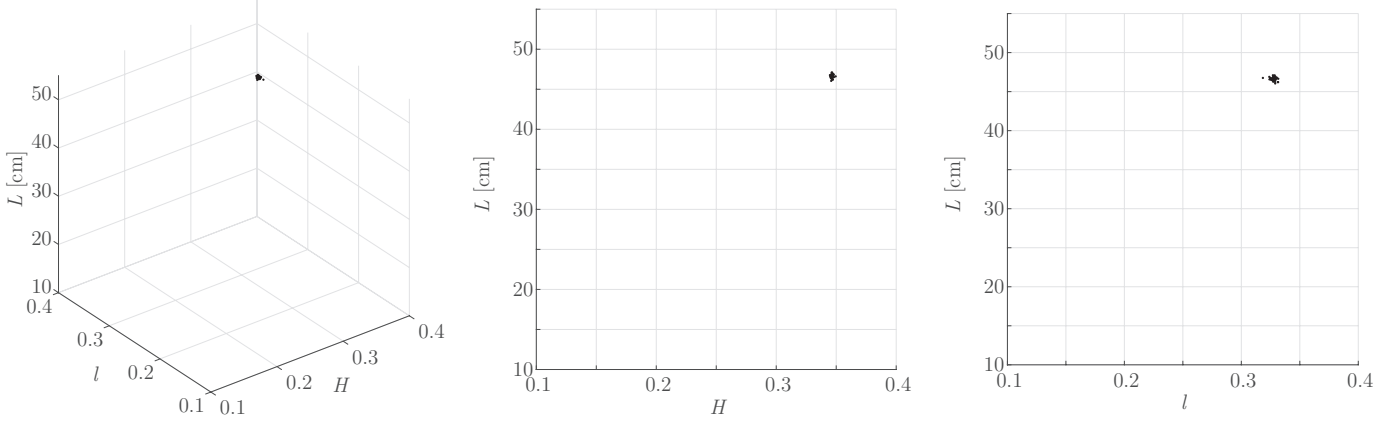


Figure 22: Optimal geometries for 100 time windows of 30 seconds without events in the $L-l-H$ space (left), $L-H$ plane (middle) and $L-l$ plane (right).

are intrinsically included in the framework and are the ones that define dissimilar results for each context. In order to highlight the impact of the occurrence rate, it is decided to include Table 5. This table contains the expected energy harvested (in a time frame of 30s) by each candidate when they are excited with events of different clusters. For example, if candidate 1 is excited with an event belonging to cluster 2, then it is expected to produce $6.10\mu\text{J}$ in 30s. As it is expected, the higher energy for an event is produced by its correlative candidate, e.g., for an event of cluster 2, the best candidate is also the number 2. Also, it is important to note that the highest energy is harvested when candidate 6 is excited with an event belonging to cluster 6. However, candidate 6 in figure 24 is the candidate that generates the lowest amount of energy accumulated in 24 hours. Contrary, it is possible to observe that the lowest amount of energy generated by any candidate occurs when no events are presented in the excitation (column 7 in Table 5). However, the candidate 7 is the one that generates the most amount of accumulated energy in 24hrs. This situation is explained by the occurrence rate of an event belonging to a specific cluster. The last row of the table incorporate the mentioned occurrence rate. Here, it is observed that events of cluster 6 have an occurrence rate close to 0.5%, while the occurrence rate for an event-less excitation is close to 95%. As it is seen, the occurrence rate plays a determinant role in the optimisation. Furthermore, the information in this table could be used to estimate the energy produced by any candidate in any time frame. For example taking candidate 1, if the first row (corresponding to candidate 1) is weighted by the occurrence rate (last row) and the result is summed, then the expected energy harvested by candidate 1 in 30s is obtained. Then, the result could be linearly scaled to estimate the expected energy harvested in a different time frame.

Table 4 compares the energy generated in this work with some previous studies. Although the results coincide with the order of magnitude, it does not exceed the harvested energy from other studies. This is mainly due to the characteristics and ways the bridge-vehicle system is modeled in these works. In particular, the fact that in [7] the research was carried out in an experimental setup with a scaled bridge-vehicle system, allows the generation of energy to occur in higher frequencies, which benefits the efficiency of the devices. On the other hand, In [10], the data used corresponds to a railway bridge, where are higher available mechanical energy compared to vehicular bridges for the greater mass and speed of trains. The same happens in [9], where the numerical simulation is modeled on a bridge-train system.

Another aspect which was not considered in this work is dependence of the optimisation results on the device's position on the bridge. In general, the device's position is associated with the different

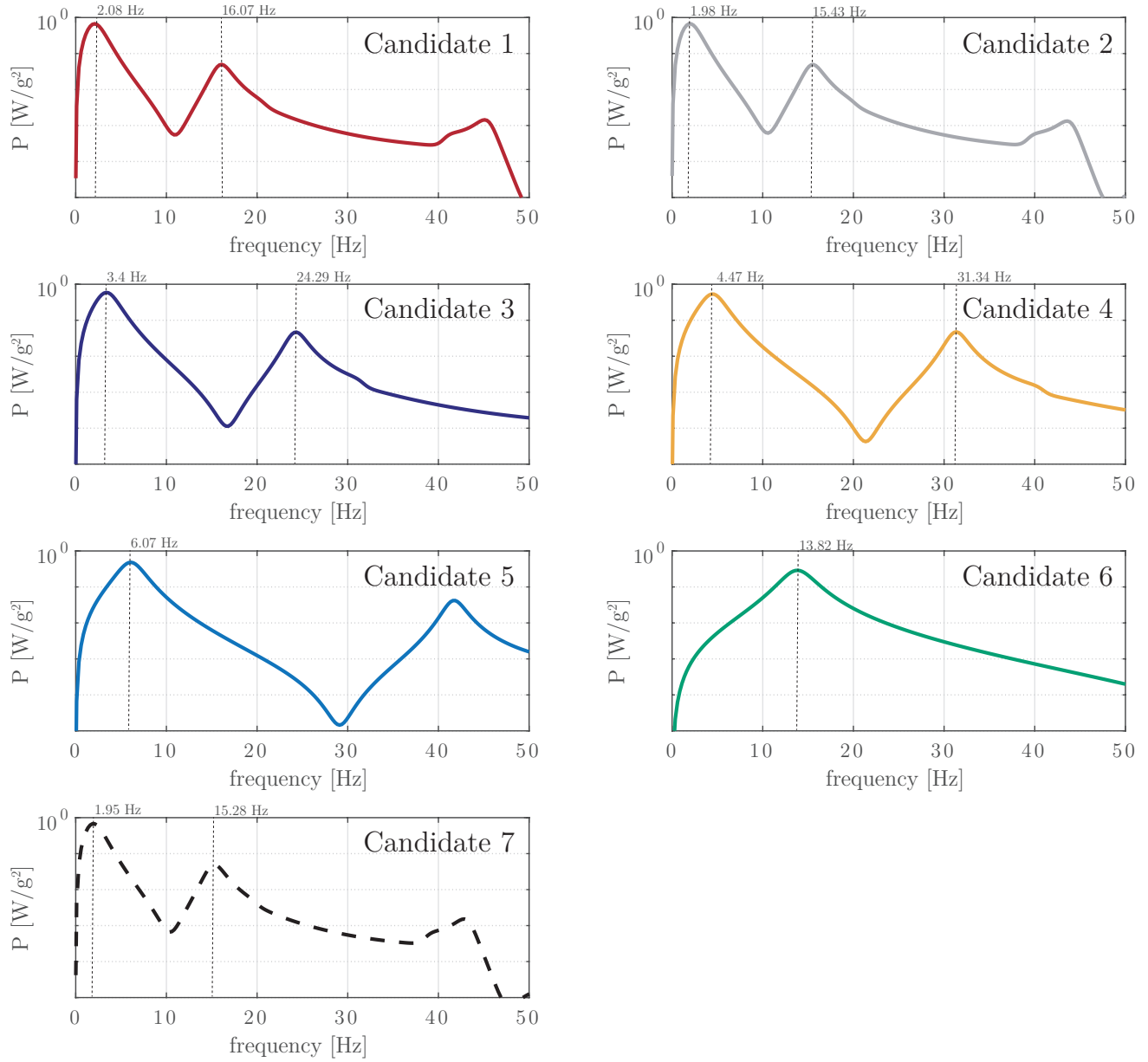


Figure 23: Power FRF of the seven candidates to assess energy harvested from a continuous 24-hour signal.

Table 4: Comparison of the harvested energy from the present work compared to some previous studies

This Work	~0-7.8 μ J	for each passing vehicle
	2.5 mJ	in 24 hours
Romero et. al [10]	3.6 mJ	for each passing train
	~0-0.84 mJ	in 3.5 hours
Song [9]	~0-462 mJ	for each passing train
Zhang et. al [7]	60-565 μ J	for each passing vehicle

vibration modes of the bridge, so the amplitude associated with specific vibration frequencies is affected. In particular, the position selected in this case study favours the first mode of vibration

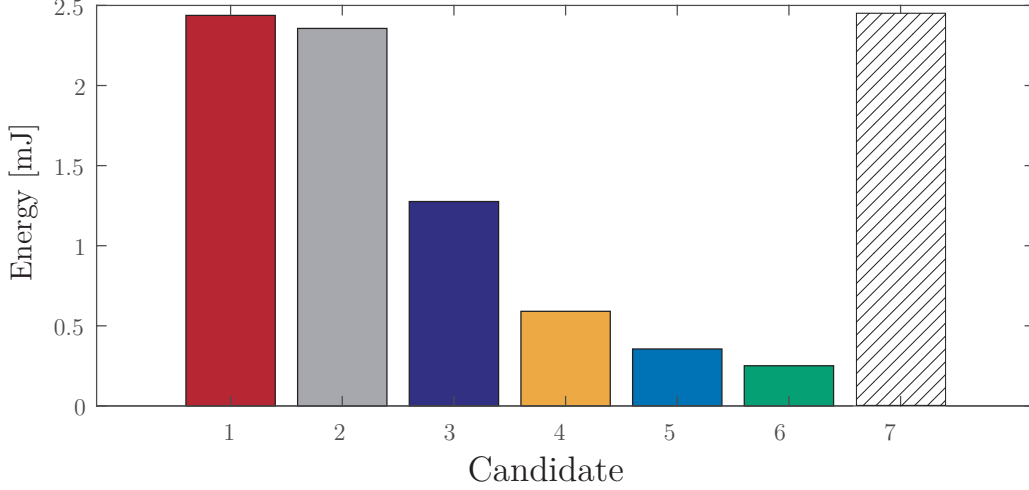


Figure 24: Energy harvested from a 24 hour signal by the seven candidates.

and explains why a more significant number of optimal devices from the individual optimisation will cluster around 2 Hz. However, it is not necessarily the optimal position on the bridge and other positions should be studied.

Table 5: Expected energy harvested (in a time frame of 30s) by all candidates when they are excited with events belonging to different clusters. The energy is in μJ . The last row corresponds to the occurrence rate of an event belonging to a particular cluster for the case study

		Event's Cluster						
		1	2	3	4	5	6	7
Candidate	1	5.50	6.10	2.13	1.40	1.06	5.43	0.54
	2	5.31	6.26	2.00	1.37	1.15	6.28	0.52
	3	3.30	3.84	2.92	1.68	1.30	3.56	0.22
	4	1.36	1.61	1.54	1.89	0.88	1.87	0.03
	5	1.86	2.29	2.11	1.74	1.43	2.56	0.07
	6	0.91	3.66	0.60	0.76	0.98	7.76	0.00
	7	5.51	6.05	2.00	1.34	1.03	5.42	0.55
Occurrence rate		0.017	0.006	0.018	0.003	0.001	0.005	0.950

6. Conclusions

This work presents a comprehensive study for the design of Piezoelectric Energy Harvesters for a bridge. The numerical PEH model is based on the Kirchhoff-love plate theory and the generalised Hamilton's principle for electroelastic bodies. Also, a modal order reduction and an efficient time integration method based on Simulink ode45 solver is presented to estimate the voltage signal from an arbitrary input acceleration signal. The approach is validated against experimental measurements.

Three shape optimisation problems and parametric studies was carried out to understand the behaviour of the PEH on a real bridge. From the studies, it was deduced that tuning the fundamental

frequency of the device with one resonance frequency of the bridge does not result in the optimal configuration, if it is evaluated for different traffic passing events in the bridge. It reveals the importance of proposing an alternative methodology to perform design optimisation.

For that purpose, an optimisation framework based on the bridge events is proposed to design a PEH, maximising the continuous power generation. The framework is performed in a real cable-stayed bridge. 1000 traffic passing events and 100 time windows without events (of 30 seconds) were considered as a representative database of the bridge. The optimal configuration was achieved from the non-event windows due to the study case's specific bridge and traffic characteristics.

The issue that is not delved into in this work, and would be interesting to explore in future works, is how the position of the PEH in the bridge affects the harvested energy. On the other hand, it would be interesting to extend the optimisation framework to the use of long time windows and compare its performance with respect to the use of (short) events in the bridge.

Acknowledgements

This research is supported by the Comision Nacional de Investigacion Cientifica y Tecnologica de Chile through the project CONICYT/FONDECYT/11180812. The authors also wish to thank CSIRO's Digital Productivity business unit, Data61 for providing the research data. The instrumentation and the field tests of this bridge have been planned and conducted by researchers at Data61 in collaboration with academics at University of New South Wales (UNSW) and Western Sydney University (WSU).

References

- [1] C. Covaci, A. Gontean, Piezoelectric energy harvesting solutions: A review, *Sensors* 20 (2020) 3512.
- [2] N. Sezer, M. Koç, A comprehensive review on the state-of-the-art of piezoelectric energy harvesting, *Nano Energy* 80 (2021) 105567.
- [3] N. Wu, B. Bao, Q. Wang, Review on engineering structural designs for efficient piezoelectric energy harvesting to obtain high power output, *Engineering Structures* 235 (2021) 112068.
- [4] M. Peigney, D. Siegert, Piezoelectric energy harvesting from traffic-induced bridge vibrations, *Smart Materials and Structures* 22 (2013) 095019.
- [5] P. Cahill, B. Hazra, R. Karoumi, A. Mathewson, V. Pakrashi, Vibration energy harvesting based monitoring of an operational bridge undergoing forced vibration and train passage, *Mechanical Systems and Signal Processing* 106 (2018) 265–283.
- [6] P. Cahill, B. Hazra, R. Karoumi, A. Mathewson, V. Pakrashi, Data of piezoelectric vibration energy harvesting of a bridge undergoing vibration testing and train passage, *Data in brief* 17 (2018) 261–266.
- [7] Z. Zhang, H. Xiang, Z. Shi, J. Zhan, Experimental investigation on piezoelectric energy harvesting from vehicle-bridge coupling vibration, *Energy Conversion and Management* 163 (2018) 169–179.
- [8] M. Karimi, A. Karimi, R. Tikani, S. Ziaei-Rad, Experimental and theoretical investigations on piezoelectric-based energy harvesting from bridge vibrations under travelling vehicles, *International Journal of Mechanical Sciences* 119 (2016) 1–11.

- [9] Y. Song, Finite-element implementation of piezoelectric energy harvesting system from vibrations of railway bridge, *Journal of Energy Engineering* 145 (2019) 04018076.
- [10] A. Romero, J. Cámara-Molina, E. Moliner, P. Galvín, M. Martínez-Rodrigo, Energy harvesting analysis in railway bridges: An approach based on modal decomposition, *Mechanical Systems and Signal Processing* 160 (2021) 107848.
- [11] C. D. M. Junior, A. Erturk, D. J. Inman, An electromechanical finite element model for piezoelectric energy harvester plates, *Journal of Sound and Vibration* 327 (2009) 9–25.
- [12] P. Peralta, R. Ruiz, S. Natarajan, E. Atroshchenko, Parametric study and shape optimization of piezoelectric energy harvesters by isogeometric analysis and kriging metamodeling, *Journal of Sound and Vibration* 484 (2020) 115521.
- [13] A. C. Hurtado, P. Peralta, R. Ruiz, M. M. Alamdari, E. Atroshchenko, Shape optimization of piezoelectric energy harvesters of variable thickness, *Journal of Sound and Vibration* 517 (2022) 116503.
- [14] K. Savarimuthu, R. Sankararajan, et al., Design and analysis of cantilever based piezoelectric vibration energy harvester, *Circuit World* (2018).
- [15] R. Hosseini, M. Nouri, Shape design optimization of unimorph piezoelectric cantilever energy harvester, *Journal of Computational Applied Mechanics* 47 (2016) 247–259.
- [16] B. Besselink, U. Tabak, A. Lutowska, N. Van de Wouw, H. Nijmeijer, D. J. Rixen, M. Hochstenbach, W. Schilders, A comparison of model reduction techniques from structural dynamics, numerical mathematics and systems and control, *Journal of Sound and Vibration* 332 (2013) 4403–4422.
- [17] J. Dormand, P. Prince, A family of embedded runge-kutta formulae, *Journal of Computational and Applied Mathematics* 6 (1980) 19–26.
- [18] P. Peralta, R. O. Ruiz, V. Meruane, Experimental study of the variations in the electromechanical properties of piezoelectric energy harvesters and their impact on the frequency response function, *Mechanical Systems and Signal Processing* 115 (2019) 469–482.
- [19] P. Peralta, R. O. Ruiz, A. A. Taflanidis, Bayesian identification of electromechanical properties in piezoelectric energy harvesters, *Mechanical Systems and Signal Processing* 141 (2020) 106506.
- [20] R. Poli, J. Kennedy, T. Blackwell, Particle swarm optimization, *Swarm intelligence* 1 (2007) 33–57.
- [21] R. E. Perez, K. Behdinan, Particle swarm approach for structural design optimization, *Computers & Structures* 85 (2007) 1579–1588.
- [22] F. Kang, J.-j. Li, Q. Xu, Damage detection based on improved particle swarm optimization using vibration data, *Applied Soft Computing* 12 (2012) 2329–2335.
- [23] T. Kanungo, D. M. Mount, N. S. Netanyahu, C. D. Piatko, R. Silverman, A. Y. Wu, An efficient k-means clustering algorithm: Analysis and implementation, *IEEE transactions on pattern analysis and machine intelligence* 24 (2002) 881–892.

- [24] A. Diez, N. L. D. Khoa, M. Makki Alamdari, Y. Wang, F. Chen, P. Runcie, A clustering approach for structural health monitoring on bridges, *Journal of Civil Structural Health Monitoring* 6 (2016) 429–445.
- [25] C. Yuan, H. Yang, Research on k-value selection method of k-means clustering algorithm, *J* 2 (2019) 226–235.
- [26] A. Erturk, D. J. Inman, A distributed parameter electromechanical model for cantilevered piezoelectric energy harvesters, *Journal of vibration and acoustics* 130 (2008) 041002.
- [27] S. Paquin, Y. St-Amant, Improving the performance of a piezoelectric energy harvester using a variable thickness beam, *Smart Materials and Structures* 19 (2010) 105020.
- [28] J. C. Lagarias, J. A. Reeds, M. H. Wright, P. E. Wright, Convergence properties of the nelder–mead simplex method in low dimensions, *SIAM Journal on Optimization* 9 (1998) 112–147.
- [29] M. M. Alamdari, N. L. Dang Khoa, Y. Wang, B. Samali, X. Zhu, A multi-way data analysis approach for structural health monitoring of a cable-stayed bridge, *Structural Health Monitoring* 18 (2019) 35–48.
- [30] M. M. Alamdari, K. Kildashti, B. Samali, H. V. Goudarzi, Damage diagnosis in bridge structures using rotation influence line: Validation on a cable-stayed bridge, *Engineering Structures* 185 (2019) 1–14.